DESIGN OF ACTIVE MAGNETIC BEARING SPINDLES FOR MICRO-MILLING APPLICATIONS

by
KAZI SHER AHMED

Submitted to the Graduate School of Engineering and Natural Sciences
in partial fulfilment of
the requirements for the degree of
Master of Science

Sabancı University
July 2021

DESIGN OF ACTIVE MAGNETIC BEARING SPINDLES FOR MICRO-MILLING APPLICATIONS

Approved by:

Date of Approval: ....

Abstract

DESIGN OF ACTIVE MAGNETIC BEARING SPINDLES FOR MICRO-MILLING APPLICATIONS

Kazi Sher Ahmed

Mechatronics Engineering, Master's Thesis, July 2021

Thesis Supervisor: Assist. Prof. Bekir Bediz

Keywords: Micro-milling, active magnetic bearing, spectral element method, multiobjective optimization, electromagnetism, surrogate optimization

The application of micro-milling for the fabrication of micro-scale parts/features from a plethora of materials has found significantly increased usage. In this fabrication process, miniaturization of mechanical components requires smaller machine tools with ultra-high rotational speeds. However, such rotational speeds complicate the spindle's dynamic response and affect the machining process's quality. Although contact or air bearings are generally used in micro-milling spindles, active magnetic bearing is a promising technology because it enables high-speed and contact-free rotation with active control of the spindle dynamics. Active magnetic bearings are being extensively studied to provide the benefits of regulated magnetic levitation and ultra-high speeds to the machining industry with condition monitoring and disturbance rejection capabilities such as chatter suppression.

The primary objective of this thesis is to design and optimize active magnetic bearing spindles for micro-milling applications and demonstrate a multiobjective optimization scheme that can be adapted to different application requirements. To achieve this objective, we developed an algorithm for the spectral element method based on the one-dimensional spectral-Chebyshev approach to predict the dynamics of high-speed spindles. Next, we developed three-dimensional finite element models for accurate performance analysis of active magnetic bearings. Afterwards, the bearing performance was optimized using gradient and nongradient-based methods. Finally, we designed the major components for spindle assembly and identified the manufacturing methods for the next steps of spindle realization.

Özet

MIKRO FREZE UYGULAMALARI IÇIN AKTIF MANYETIK YATAK MILLERININ TASARIMI

Kazi Sher Ahmed

Mekatronik Mühendisliği ,Yüksek Lisans Tezi, Temmuz 2021

Tez Danışmanı: Assist. Prof. Bekir Bediz

Anahtar Kelimeler: Mikro frezeleme, aktif manyetik rulmanlar, spektral eleman yöntemi, çok amaçlı optimizasyon, elektromanyetizma, vekil optimizasyon

Çok sayıda malzemeden mikro ölçekli parçaların/özelliklerin üretimi için mikro frezeleme uygulaması, kullanımı önemli ölçüde artırmıştır. Bu üretim sürecinde, mekanik bileşenlerin minyatürleştirilmesi, ultra yüksek dönüş hızlarına sahip daha küçük takım tezgahları gerektirir. Ancak, bu tür dönüş hızları iş milinin dinamik tepkisini zorlaştırır ve işleme sürecinin kalitesini etkiler. Mikro freze iğlerinde genellikle temaslı veya havalı yataklar kullanılmasına rağmen, aktif manyetik yatak, iş mili dinamiklerinin aktif kontrolü ile yüksek hızlı ve temassız dönüş sağladığı için umut verici bir teknolojidir. Aktif manyetik yataklar, talaş kaldırma gibi durum izleme ve bozulma reddetme yetenekleriyle işleme endüstrisine düzenlenmiş manyetik kaldırma ve ultra yüksek hızların faydalarını sağlamak için kapsamlı bir şekilde araştırılmaktadır.

Bu tezin birincil amacı, mikro frezeleme uygulamaları için aktif manyetik yataklı milleri tasarlamak ve optimize etmek ve farklı uygulama gereksinimlerine uyarlanabilen çok amaçlı bir optimizasyon şemasını göstermektir. Bu amaca ulaşmak için, yüksek hızlı iğlerin dinamiklerini tahmin etmek için tek boyutlu spektral-Chebyshev yaklaşımına dayanan spektral eleman yöntemi için bir algoritma geliştirdik. Ardından, aktif manyetik yatakların doğru performans analizi için üç boyutlu sonlu eleman modelleri geliştirdik. Daha sonra, gradyan ve gradyan tabanlı olmayan yöntemler kullanılarak rulman performansı optimize edildi. Son olarak, iş mili montajı için ana bileşenleri tasarladık ve iş mili gerçekleştirmenin sonraki adımları için üretim yöntemlerini belirledik.

Acknowledgements

I would like to express my deep gratitude to my advisor, Dr. Bekir Bediz for guiding me with enthusiasm and patience and giving me freedom to explore throughout my studies.

Dr. Güllü Kızıltaş Şendur for her well-designed courses on multiobjective optimization and for her guidance during thesis studies.

Dr. Recep Önler for his review of the thesis and valuable suggestions.

İlker Sevgen and Barış Tümer for their support with laboratory equipment and resources.

And finally, my friends in the lab: Meisam, Peiman, Dilara, Ender, Andisheh, Ece, and Saeed for their support and friendship.

To my parents,
for their love and patience.

Table of Contents

List of Tables

List of Figures

Chapter 1

Introduction

Chapter 1 discusses the application of micro-milling to address the growing demands of miniaturized components. It further elaborates on the benefits of using active magnetic bearing (AMB) in micro-milling spindles. The design and performance optimization of AMBs aided by finite element (FE) modelling is an important goal of this thesis.

1.1 Miniaturization and Micro-Machining Processes

There has been an increasing demand for (complex) three-dimensional (3D) components with micro-scale features, especially in the fields of bio-engineering, aerospace, energy conversion, and robotics [1, 2]. Functionality, material savings, small dimensions, and reduced masses motivate the miniaturization of components. In addition to being a well-established need of industrial sectors, the focus on miniaturization also aligns with the recently published European Union missions and policies on climate change [3, 4]. In this context, miniaturized products require less specific energy.

To fabricate these micro-scale features, various micro-manufacturing techniques/approaches have been developed. In general micro-manufacturing can be classified into two types: lithography and non-lithography methods [5]. Within lithography-based techniques, photolithography is the key fabrication method, but it has certain limitations in terms of material and geometry capabilities. Fabricating complex 3D (high-aspect) ratio features can be impractical and costly. To address these issues (*i.e.* to overcome these limitations), non-lithography methods such as mechanical micromachining are used. Benefits are present in terms of freedom of material selection, intricate part geometry, relative accuracy, and cost efficiency.

Mechanical micro-milling, which is basically the scaled-down version of macro-scale mechanical milling process, is a promising versatile micro-fabrication process for micro-scale parts/components. This technique can be used to fabricate complex 3D (free-form) features on a broad range of materials, including polymers, ceramics, and metals [6–8]. There are three main elements of a micro milling-tool (μMT): **(i)** a micro-scale cutting tool (whose diameter can go down to 50 μm), **(ii)** a miniature ultra-high-speed (UHS) spindle, and **(iii)** high-precision stages to provide relative motion between the workpiece and the cutting tool. Although mechanical micro-milling is a promising approach, its full potential has not been realized yet since it is not that straightforward to relate the process parameters with the performance metrics due to the size effects.

One of the main issues that hinders the exploitation of the potentials of this process is arising from the bearings that are used in commercially available systems. Initially, contact bearing systems are used in miniature spindles, however, due to the continuous contact, there are problems such as heating (leads to thermal deformation) and spindle speed limitations [9]. More recently, air bearings are implemented and rotational speeds up to 400,000 rpm can be achieved [10]. Although ultra high rotational speeds can be achieved with air bearings, it is a passive system; thus the spindle error motions, that are radial, axial, and tilt motions of the spindle) are the main problems since they leads to low process accuracy.

To overcome these limitations, AMBs seem a promising approach since it allows high rotation speeds required by the process and high accuracy since it enables monitoring the process and thereby controlling the micro-tool motions to increase the positional accuracy [9].

1.2 Active Magnetic Bearings in Micro-Milling Spindles

Micro-milling spindles require relatively very high rotational speeds (above 60,000 rpm) compared to the macro-scale milling machines to provide the same quality of machining and tool edge cutting speed (*i.e.*, to achieve process quality and efficiency) [11]. In conventional bearings, the mechanical contact between stator-rotor limits the rotational speed due to heat generation and deformation. In contrast, AMBs enable a non-contact, lubrication-free, energy-efficient, and ultra-high speed rotation with an ability to control the spindle dynamics [12]. Among machining-focused implementations of AMBs, Kimman *et al.* [9] realized a miniature milling spindle supported by permanent magnet (PM) biased homopolar magnetic bearings with a target speed of 150,000 rpm. The spindle was driven by a commercial permanent magnet synchronous motor. Park *et al.* [13] constructed a prototype of an air-turbine driven miniature spindle that reached up to 200,000 rpm with a tool orbit of less than 10 μm. Knospe [14] experimented with two AMB test-rigs for active suppression of machining chatter.

Typical AMB-supported spindles involve slender and stepped rotors. The stepped segments of the rotor are necessary to accommodate spatially separated components including radial bearings, sensors, backup bearings, axial bearing, and motor drive. Many AMB spindles are based on this configuration. However, in line with miniaturization of micro-machining devices, a significant reduction in rotor slenderness shifts the flexural (bending) resonances out of the operating range; thereby prevents resonance due to machining excitation [15]. Such a design necessitates a compact integration of the spindle components with a combined radial-axial AMB as conceived by Lee [16] and later analysed by Kimman [15] for a five-degree-of-freedom (5-DOF) control of a short rotor.

1.3 Modeling Methods for Active Magnetic Bearing Spindles

This section describes the modelling techniques for the rotor and bearing components of the spindle.

1.3.1 Modeling the rotor dynamics

The dynamic behavior of the machine tool system reflected at the tool tip dictates the achievable process efficiency and quality. One of the critical elements that affect the tool tip dynamics is the spindle. Furthermore, as mentioned above, the micro-milling spindles rotate at relatively high rotational speeds, the dynamics of the system may change significantly as a function of the spindle speed. Therefore, to design a micro-milling spindle, the speed-dependent dynamics of the spindle rotor needs to be analyzed to accurately predict the response of the system and decrease the unwanted vibrations that may limit the process quality and productivity.

The rotor has a sectioned geometry composed of simple circular cross-sections leading to uncoupled axial, torsional, and bending motions [17]. Therefore, in the literature, common beam-based methods such as Euler-Bernoulli beam approach [18] and Timoshenko beam approach [19], are used to model the rotordynamics (that is basically a spinning beam). The beam-based methods can be classified based on the kinematic equations used for the deformation of the beam. Note that the rotor of the micromilling spindles is composed of stubby sections, therefore Euler-Bernoulli beam approach may not capture the dynamics of the rotor accurately since the shear and rotary effects are not included. Thus, Timoshenko beam approach is the prevailing method used in literature. Cao and Altintas [20], using finite elements, developed a general modeling approach including the centrifugal force and gyroscopic effects to determine the spindle dynamics. Although the FE approach leads to accurate results, its main drawbacks are the mesh convergence and computational burden [21]. To overcome the limitations of FE methods, Erturk *et al.* [22, 23] used the Timoshenko beam modeling approach to model the spindle dynamics using a receptance coupling approach.

To increase the computational efficiency in modeling approaches, series based methods are getting popular such as Differential Quadrature Method [24, 25] and spectral Chebyshev approach [26, 27]. If the polynomials used in expressing the deflections have exponential convergence such as Fourier series and Chebyshev polynomials, accurate results can be obtained using very few degrees of freedom [28]. However, the main drawback of the spectral methods is that the geometry should be continuous. To overcome this limitation, in this study, we developed a spectral element method based on Timoshenko beam modeling approach. Thus, each segment of the rotor can be modeled individually and the system matrices of each section can be used to obtain the overall system matrices to analyze the speed-dependent dynamics of the system.

1.3.2 Modeling active magnetic bearings

Conventionally, AMBs have been modelled analytically, and the necessary dimensions are determined based on certain rules of thumb accepted in industry and academia [29]. In most of the analytical models, it is assumed that no leakage flux and hysteresis occur. Furthermore, infinite permeability of iron and absence of flux saturation are commonly assumed in the modelling process. These assumptions, coupled with correction factors based on experience or experiments, have been largely accepted in design and optimization of AMBs [30]. For instance, Han *et al.* [30] optimized a combined radial-axial magnetic bearing for a compressor application using an integrated optimization method. Another important study was carried out by Le and Wang [31] where they considered the eddy current and leakage effects while optimizing a combined magnetic bearing for high-speed motors following a weighted sum approach and sequential quadratic programming algorithm.

While analytical models are computationally inexpensive in optimization studies, they are inaccurate in compact designs where flux leakage, nonlinear nature of magnetic flux density-magnetic field intensity (B-H) curves, and saturation effects are prominent enough to affect the bearing performance. In the short rotor design analysed by Kimman [15], the air-gap flux densities from analytical and FE models differed as much as 50%, rendering the assumptions incorrect and mandating a more accurate model, such as an FE model. In this regard, Ding *et al.* [32] presented an optimal design of a radial bearing for hard disk drives. Later, Cheng *et al.* [33] optimized a hybrid magnetic bearing for heart pumps using a 3D FE-based optimization.

1.4 FE-Based Multi-Objective Optimization

In favor of the increased accuracy needed for a compact design where flux leakage and saturation effects are not negligible, FE model is preferred to aid the performance optimization. The initial design is developed in response to high-speed milling requirements (defined in detail in Section 4.1), and to accommodate motor integration as an important next step. The initial sizing ensures that the magnetic flux paths do not become saturated when maximum current excitation is applied.

1.5 Thesis Objectives and Contributions

The mechanical micromachining requires ultra-high rotational speeds to provide acceptable quality for machined parts. The use of conventional bearings in micromilling machines limits achievable speeds due to thermal deformation. AMB is a promising technology to achieve ultra-high speeds and positional accuracy without stator-rotor contact. Advantages of AMBs include low machine maintenance costs, active compensation of disturbances during operation, and process/condition monitoring.

The conventionally used analytical AMB design methods are less accurate when compared with 3D FE models, particularly for compact designs where flux leakage, non-linear magnetization, and saturation effects are prominent. Moreover, several parameters define the performance of an AMB. These performance parameters can have different hierarchy levels for different target applications. This guides to the objectives of this thesis to **design active magnetic bearing spindles based on accurate three-dimensional finite element models and demonstrate an optimization scheme which can be adapted based on different application requirements**.

To meet the objectives, the main contributions of this thesis are focused on the design and performance optimization of AMB-supported micro-milling spindles. Specifically:

A. Development of spectral element method based on one-dimensional (1D) spectral-Chebyshev (ST) approach to predict the dynamics of high-speed spindles. This element approach also allows convenient placement of components such as bearings and discs on the rotor.

B. Development of 3D FE-based models for accurate performance analysis of AMBs.

C. FE-based performance optimization of bearing using gradient and nongradient optimization methods.

D. Design of spindle assembly, identification of manufacturing methods, and development of machining drawings for the next step of spindle realization.

1.6 Thesis Outline

The thesis is organized as follows:

- A precise prediction of the dynamic response of high-speed rotors in micro-milling spindles is of paramount importance at the design stage. To be able to successfully predict this rotordynamic response and make design adjustments accordingly, **Chapter** 2 describes an spectral element method based on Timoshenko beam theory. It further explains the code algorithm to model stepped rotors with discs and bearings.

- Considering several AMB topologies suited for different applications, **Chapter** 3 justifies two different topologies for micro-milling applications: (**1**) miniaturized combined radial-axial bearing spindle and (**2**) relatively larger, slender rotor spindle with separate axial and radial bearings. The analytical and finite element modelling is presented next, which forms the basis for design and optimization process in later chapters.

- **Chapter** 4 establishes micro-milling application requirements for the initial design and subsequent multiobjective performance optimization of AMBs. Based on the models developed in Chapter 3, the miniaturised spindle topology is dimensioned to meet the application requirements. Afterwards, single and multiobjective optimizations, using gradient and nongradient methods, are performed to improve the performance of bearings.

- With miniaturized spindle dimensioned and optimized, we now treat a slightly larger spindle with a slender rotor. **Chapter** 5 presents the design of major components of such a spindle with a focus on manufacturing as an immediate next step building on this thesis.

- Finally, the thesis is concluded in **Chapter** 6 with recommendations on manufacturing and experimentation for future work.

Chapter 2

Spectral Element Modelling for Rotordynamical Analysis

A high-speed rotor is one of the primary elements of a micromilling spindle. The speed-dependent dynamics become more prominent and vibration issues are amplified at higher rotational speeds. Therefore, a precise prediction of the rotordynamic response is necessary at the design phase. This predicted response, through an accurate model, enables design modifications for a stable rotor function within operating speeds. Additionally, in AMB-supported rotor systems, this model aids the development of model-based levitation controllers [34].

While FE models are highly accurate for rotordynamics, they carry a computational cost when the structure becomes complex [26]. For increased computational efficiency, series-based methods such as differential quadrature method and spectral Chebyshev approach are gaining traction. As explained in Section 1.3.1, we developed an algorithm for spectral element method using Timoshenko beam theory and exponentially converging Chebyshev polynomials. This allowed us to conveniently integrate system components such as bearings and discs in the model for the analysis of speed-dependent system dynamics. This chapter describes a summary of the Timoshenko beam equations and the details of the spectral element method.

2.1 Timoshenko Beam Theory

As opposed to Euler-Bernoulli beam model, Timoshenko beam model includes shear deformation and rotational inertia effects. This makes the latter more accurate for determining the dynamic response at higher frequencies and for beams with lower slenderness (ratio of the square of beam length and radius of gyration of the cross-section) [35].

In this model based on one-dimensional spectral-Chebyshev approach, bending, axial, and torsional deformations are taken into account. The integral form of the boundary value problem (IBVP) is derived using the extended Hamilton's principle [36] which is stated as

$$\int_{t_1}^{t_2} (\delta T - \delta V + \delta W_{\mathrm{nc}})\, \mathrm{d}t = 0, \quad \delta q_i = 0 \quad \text{at} \quad t = t_1, t_2 \tag{2.1}$$

where T, V, and W_{nc} are the kinetic energy, strain (potential) energy, and the work done by non-conservative forces, respectively. Two instants of time are given by t_1 and t_2. The generalised coordinate q_i corresponds to the i^{th} term of the displacement vector

$$\mathbf{q} = \{w_x;\, w_y;\, w_z;\, \psi_x;\, \psi_y;\, \psi_z\} \tag{2.2}$$

which packs six degrees of freedom: three linear displacements and three rotational displacements about the cross-sectional axis. For a beam based on Timoshenko theory, the strain (potential) energy for an axisymmetric beam is written as

$$\begin{aligned} V = \frac{1}{2}\int_0^L \Bigg\{ & EI_{xx}(z)\left(\frac{\partial \psi_x}{\partial z}\right)^2 + EI_{yy}(z)\left(\frac{\partial \psi_y}{\partial z}\right)^2 \\ & + 2EI_{xy}\left(\frac{\partial \psi_x}{\partial z}\right)\left(\frac{\partial \psi_x}{\partial z}\right) \\ & + kA(z)G\left[\left(\frac{\partial w_x}{\partial z} - \psi_y\right)^2 + \left(\frac{\partial w_y}{\partial z} + \psi_x\right)^2\right] \\ & + EA(z)\left(\frac{\partial w_z}{\partial z}\right)^2 + GJ(z)\left(\frac{\partial \psi_z}{\partial z}\right)^2 \Bigg\}\mathrm{d}z \end{aligned} \tag{2.3}$$

where L is beam's length, E is the Young's modulus, $I_{xx}(z)$ is cross-sectional moment of inertia with respect to x axis, $I_{yy}(z)$ is cross-sectional moment of inertia with respect to y axis, $I_{xy}(z)$ is the product of inertia, k is the shear constant, $A(z)$ is beam's area along the z axis, G is a dimensionless shear modulus based on cross-section geometry, and $J(z)$ is the polar moment of inertia.

Next, the kinetic energy is formulated as the sum of translational T_{t} and rotational

T_{r} terms (to capture rotary effects) and is given by

$$\begin{aligned} T &= T_{\mathrm{r}} + T_{\mathrm{t}} \\ &= \frac{1}{2}\int_0^L \rho\left[I_{xx}(z)\omega_1^2 + 2I_{xy}\omega_1\omega_2 + I_{yy}(z)\omega_2^2 + J(z)\omega_3^2\right]\mathrm{d}z \\ &+ \frac{1}{2}\int_0^L \rho A(z)\left(\mathbf{v}_{\mathrm{D}}\cdot\mathbf{v}_{\mathrm{D}}\right)\mathrm{d}z \end{aligned} \tag{2.4}$$

where ρ is beam's density, $\mathbf{v}_{\mathrm{D}}$ is velocity of any point along the length of beam (bold letter denoting a vector quantity), w_1, w_2, and w_3 are the components of rotational velocity vector w_{r} applied to tool cross-section centre on the $t_1t_2t_3$ frame undergoing rotary vibrations (refer to Fig. S12 in supplementary material of Bediz and Ozdoganlar [17]). Next, the velocity vector $\mathbf{v}_{\mathrm{D}}$ is derived in terms of deflection and rotational velocities. For details, the readers are referred to Bediz *et al.* [26] and Filiz *et al.* [37].

The work done by non-conservative forces is stated as

$$W_{\mathrm{nc}} = \int_0^L \left(f_x^{\mathrm{T}} w_x + f_y^{\mathrm{T}} w_y + f_z^{\mathrm{T}} w_z\right)\mathrm{d}z \tag{2.5}$$

where f_x, f_y, and f_z are external forces aligned in x, y, and z directions, respectively.

With the kinetic energy, strain energy, and the work done by non-conservative forces derived, we use the extended Hamilton's principle given in Eq. (2.1) to obtain the IBVP for 1D beam as

$$\begin{aligned} &\int_{t_1}^{t_2}\left\{\int_0^L \left\{\rho\ddot{\mathbf{q}}^{\mathrm{T}}\mathbf{N}_{\mathrm{M}}\delta\mathbf{q} + 2\rho\Omega\dot{\mathbf{q}}^{\mathrm{T}}\mathbf{N}_{\mathrm{C_{cor}}}\delta\mathbf{q} + \mathbf{q}^{\mathrm{T}}\mathbf{N}_{\mathrm{K}}\delta\mathbf{q}\right.\right. \\ &-\rho\Omega^2\mathbf{q}^{\mathrm{T}}\mathbf{N}_{\mathrm{K_{spin}}}\delta\mathbf{q} - \rho\Omega^2\mathbf{q}_{\mathrm{ip}}{}^{\mathrm{T}}\mathbf{N}_{\mathrm{F_c}}\delta\mathbf{q} - \mathbf{n}_{\mathrm{F_c}}^{\mathrm{T}}\delta\mathbf{q} \\ &\left.\left.-f_x^{\mathrm{T}}\delta w_x - f_y^{\mathrm{T}}\delta w_y - f_z^{\mathrm{T}}\delta w_z\right\}\mathrm{d}z\right\}\mathrm{d}t = 0 \end{aligned} \tag{2.6}$$

where $\mathbf{q}_{\mathrm{ip}} = \{\mathbf{0};\ \mathbf{0};\ \mathbf{z};\ \mathbf{0};\ \mathbf{0};\ \mathbf{0}\}$ is the vector of initial positions for each point along the beam axis; $\mathbf{N}_{\mathrm{M}}$ and $\mathbf{N}_{\mathrm{K}}$ represent the operator system matrices for mass and stiffness matrices, respectively; $\mathbf{N}_{\mathrm{C_{cor}}}$ $\mathbf{N}_{\mathrm{K_{spin}}}$, and $\mathbf{N}_{\mathrm{F_c}}$ are operator system matrices related to rotational effects of the Coriolis forces, the spin-softening (centrifugal-softening) effect, and the centrifugal forces, respectively; and $\mathbf{n}_{\mathrm{F_c}}$ is the vector arising from the centrifugal forces. These operator system matrices are given in supplementary material in Bediz and Ozdoganlar [17].

2.2 One-Dimensional Spectral-Chebyshev Technique

For solution of the derived IBVP, 1D spectral-Chebyshev technique [27] will be used to spatially discretize Eq. (2.6). This involves the use of Chebyshev series expansion with representation of the derivatives and inner products as Chebyshev matrices. Chebyshev polynomials are defined as a set of recursive and orthogonal polynomials [38] given as

$$T_k(x) = \cos\left(k\cos^{-1}(x)\right) \qquad \text{for integer } \; k = 0, 1, 2, \cdots \tag{2.7}$$

These polynomials (functions) are defined for all x values but are a stable representation (form a complete set) only for the interval $(-1, 1)$. In other words, any square-integrable function can be expressed in an exact manner by an infinite series expansion with Chebyshev polynomials as the basis. However, in applications such as modelling a beam, the physical dimensions may be better expressed in the interval (l_1, l_2) instead of $(-1, 1)$. Therefore, a linear mapping (scaling) is established between the two intervals $x \in (l_1, l_2)$ and $\xi \in (-1, 1)$ as

$$x(\xi) = \frac{\ell_2 - \ell_1}{2}\xi + \frac{\ell_1 + \ell_2}{2} \tag{2.8}$$

$$\xi(x) = \frac{2}{\ell_2 - \ell_1}x - \frac{\ell_1 + \ell_2}{\ell_2 - \ell_1} \tag{2.9}$$

This allows us to use the scaled Chebyshev polynomials $\mathbb{T}_k(x) = T_k(\xi(x))$ when considering functions on the interval (l_1, l_2). Now a function $y(x) \in (l_1, l_2)$ can be written using Chebyshev series expansion as

$$y(x) = \sum_{k=0}^{\infty} a_k \mathbb{T}_k(x) \tag{2.10}$$

The coefficients a_k in the Chebyshev expansion will decay exponentially with an increasing value of k if the square-integrable function $y(x)$ is infinitely differentiable on the interval (l_1, l_2). Consequently, if a function $y(x)$ is well-behaved (no narrow spikes or regions with very large derivates) on the interval (l_1, l_2), a finite number of terms can accurately represent the function [27] for numerical calculations as

$$y_N(x) = \sum_{k=0}^{N-1} a_k \mathbb{T}_k(x) \tag{2.11}$$

where N is the number of polynomials utilized in the truncated expansion. Due to the exponential convergence nature of Chebyshev expansion, functions can be represented accurately with a low number of polynomials and the error from the truncation can be estimated.

2.3 Gauss-Lobatto Sampling

For calculations, while it is possible to sample a continuous function at N arbitrary spatial points, the following two sampling approaches are suitable for Chebyshev polynomials: (**1**) Gauss-Chebyshev sampling, (**2**) Gauss-Lobatto sampling. Adopting the second option, the Gauss-Lobatto sampling points p_k are given by:

$$p_k = \cos\left(\frac{(k-1)\pi}{N-1}\right), \quad k = 1, 2, 3, \cdots, N \tag{2.12}$$

With the condition that a function can be represented by N Chebyshev polynomials and sampled spatially at N points $\{x_k\}_{k=1}^{N}$, the Chebyshev expansion coefficients a_k and sampled function points $y_k = y(x_k)$ can be related with a one-to-one mapping [27] as

$$\left\{ \begin{array}{c} y_0 \\ y_1 \\ \vdots \\ y_{N-1} \end{array} \right\} = \left[\begin{array}{cccc} \mathbb{T}_0(x_0) & \mathbb{T}_1(x_0) & \cdots & \tau_{N-1}(x_0) \\ \mathbb{T}_0(x_1) & \mathbb{T}_1(x_1) & \cdots & \tau_{N-1}(x_1) \\ \vdots & \vdots & \ddots & \vdots \\ \mathbb{T}_0(x_{N-1}) & \mathbb{T}_1(x_{N-1}) & \cdots & \mathbb{T}_{N-1}(x_{N-1}) \end{array} \right] \left\{ \begin{array}{c} a_0 \\ a_1 \\ \vdots \\ a_{N-1} \end{array} \right\} \tag{2.13}$$

Expressing this in the matrix form as

$$\mathbf{y} = \mathbf{\Gamma}_{\mathrm{B}} \mathbf{a} \tag{2.14}$$

where $\mathbf{y}$, $\mathbf{\Gamma}_{\mathrm{B}}$, and $\mathbf{a}$ denote the vector of sampled function, the NxN backward transformation matrix, and the vector of Chebyshev expansion coefficients, respectively. Similarly, a forward transformation matrix is given by

$$\mathbf{a} = \mathbf{\Gamma}_{\mathrm{F}}\mathbf{y} \tag{2.15}$$

It should be noted that $\mathbf{\Gamma}_{\mathrm{B}}\mathbf{\Gamma}_{\mathrm{F}} = \mathbf{\Gamma}_{\mathrm{F}}\mathbf{\Gamma}_{\mathrm{B}} = \mathbf{I}$, where $\mathbf{I}$ is an NxN identity matrix.

2.4 Equation of Motion

We sampled the generalised coordinates defined in the displacement vector $\mathbf{q}$ (refer to Eq. (2.2)) in the spatial domain and represent them using truncated Chebyshev polynomial expansion as

$$q_i(z,t) \cong \sum_{k=0}^{N-1} a_i(t)\mathbb{T}_k(z) \tag{2.16}$$

where $\mathbb{T}_k(z)$ are the scaled Chebyshev polynomials, N is the number of polynomials used in the expansion, and a_i are time-dependent coefficients of expansion [17]. In a similar manner to Eqs. (2.14-2.15), the vector of sampled function $\mathbf{q}$ and the vector of expansion coefficients $\mathbf{a}$ can be related as

$$\mathbf{q} = \mathbf{\Gamma}_{\mathrm{B}}\mathbf{a} \quad \text{and} \quad \mathbf{a} = \mathbf{\Gamma}_{\mathrm{F}}\mathbf{q} \tag{2.17}$$

Next, n^{th} spatial derivative of $\mathbf{q}$ can be written as

$$\mathbf{q}_i^n = \mathbf{Q}_n\mathbf{q}_i \tag{2.18}$$

where $\mathbf{Q}_n$ is the n^{th} derivative matrix derived using backward and forward transformation matrices [27]. An inner product of $f(x)$ and $g(x)$ can be written as

$$\int_a^b r(x)f(x)g(x)\mathrm{d}x = \mathbf{f}^{\mathrm{T}}\mathbf{V}^{\mathbf{r}}\mathbf{g} \tag{2.19}$$

where $r(x)$ denotes the weighing function, and $\mathbf{V}^{\mathbf{r}}$ is the weighted inner product matrix [27]. Afterwards, the global matrices can be used to write the discretized deflections as

$$\mathbf{v} = [\,\mathbf{O}\,\mathbf{I}\,\mathbf{O}\,\mathbf{O}\,\mathbf{O}\,\mathbf{O}\,]\,\mathbf{q} = \mathbf{I}_v\mathbf{q} \tag{2.20}$$

$$\boldsymbol{\psi}_z = [\,\mathbf{O}\,\mathbf{O}\,\mathbf{O}\,\mathbf{O}\,\mathbf{O}\,\mathbf{I}\,]\,\mathbf{q} = \mathbf{I}_{\psi_z}\mathbf{q} \tag{2.21}$$

where $\mathbf{I}$ and $\mathbf{O}$ are NxN identity and zero matrices, respectively. With the deflections discretized and applying the derivative and inner product operations, we derived the equation of motion as

$$\mathbf{M}\ddot{\mathbf{q}} + (\mathbf{C} + \mathbf{C}_{\mathrm{cor}})\,\dot{\mathbf{q}} + (\mathbf{K} - \mathbf{K}_{\mathrm{spin}}\,)\,\mathbf{q} = \mathbf{f} \tag{2.22}$$

where $\mathbf{M}$, $\mathbf{C}$, $\mathbf{C}_{\mathrm{cor}}$, $\mathbf{K}$, $\mathbf{K}_{\mathrm{spin}}$, and $\mathbf{f}$ are the mass, damping, Coriolis, spin-softening (centrifugal softening) matrices and the force vector, respectively. Afterwards, the state-space formulation is used and the eigenvalues and eigenfrequencies of the system matrix are obtained to study the speed-dependent dynamics of the system.

2.5 Spectral Element Method Algorithm

Continuing with the results from previous sections, the algorithm of 1D spectral element method (SEM) for Timoshenko rotating beam is summarised below.

- Rotor geometrical and mechanical properties along with the number of spatial divisions required for Chebyshev polynomials are defined by the user. Alternatively, the number of Chebyshev polynomials can also be determined using the specified length-to-diameter ratio for each rotor segment (the definition of segment follows next).
- Next, the rotor is divided into segments. A new segment is defined whenever the diameter is changed or components such as bearing and discs are present.
- The polar and diametral mass moments of inertia and mass of discs are calculated.
- Next, the numbers of polynomials are calculated for each segment.

- Based on the number of polynomials and segments, the global system matrices are declared.
- A segment-by-segment build-up of global matrices takes place in a loop. The forward and backward transformation matrices, derivative, and inner product matrices are formed.
- Next, the positions of the degree of freedoms are rearranged so that global assembly of segment matrices is not complicated.
- Segment stiffness, mass, and Coriolis matrices are filled in and placed at the right position in the global matrices.
- The loop moves on to the next segment and the aforementioned procedure repeats.
- Once the global matrices have been formed, the disc and bearing dynamics are added at the relevant nodal locations.
- Finally, the eigenvalue problem is solved using the command *eig* in MATLAB.
- The eigenvalues and eigenvectors are postprocessed to get the results including mode shapes and Campbell diagrams.

2.6 Example Problem

The rotor geometry used by Ahmed and Ahmad [39] is modelled using the SEM code and the schematic is shown in Fig. 2.1. As noticed, this rotor consists of a stepped shaft with three discs and two bearings.

The elastic modulus of shaft is kept at $2.07\text{x}10^{11}$ N/m^2. The density of rotor and disc material is 7.83 kg/m^3. A Poisson's ratio of 0.33, shear modulus of $8.27\text{x}10^{10}$ N/m^2, and shear factor of 1.128 are used. To determined the number of polynomials for each segment, a length-to-diameter ratio of 0.4 is used.

As a example analysis, the Campbell diagram to study the speed-dependent dynamics of the rotor is shown in Fig. 2.2

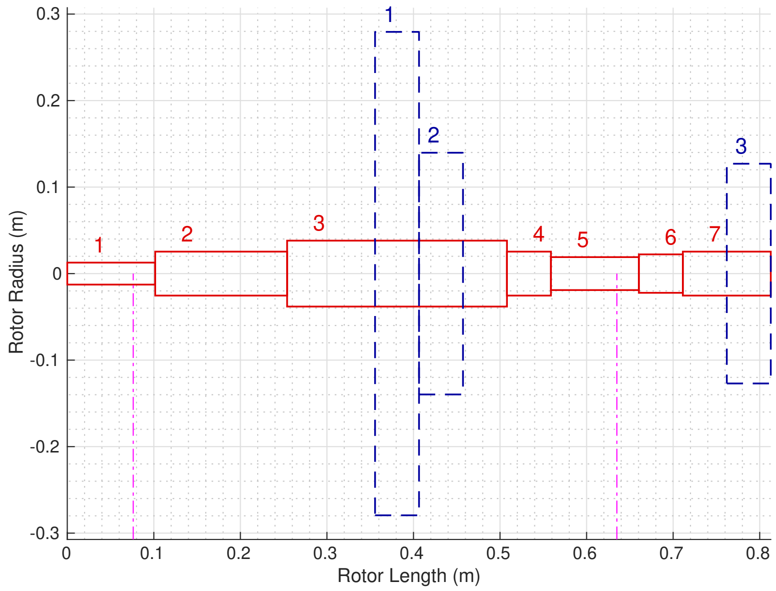

Figure 2.1: Rotor schematic with shaft sections in red and three discs in blue. The bearing locations are represented with pink dash-dotted lines.

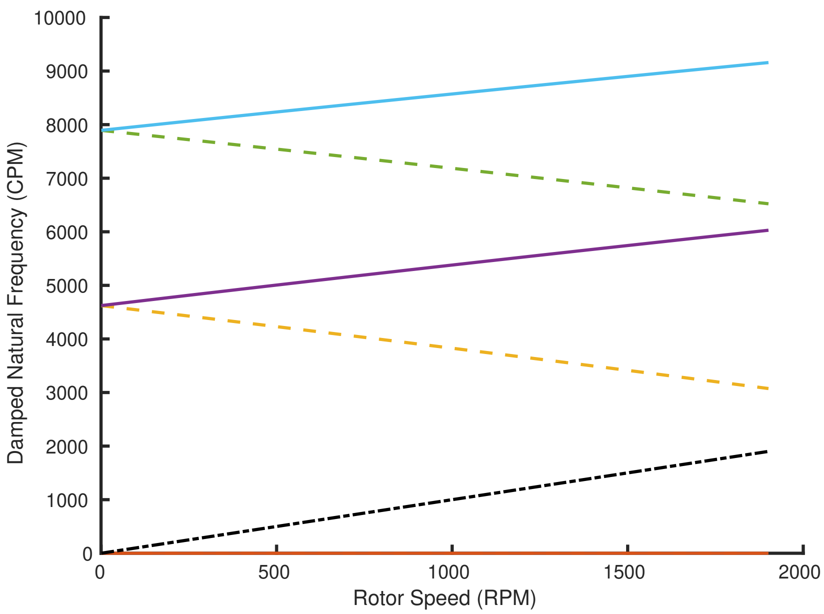

Figure 2.2: Campbell diagram showing variation of natural frequencies in cycles per minutes with the rotor speed in revolutions per minute. The dashed lines show the backward modes. 1X speed line is shown in black dashes.

2.7 Summary

This chapter elaborates on an spectral element model method and algorithm based on Timoshenko beam theory and Chebyshev polynomials. The algorithm of the developed code summarizes the primary steps from user input to the final evaluation of eigenvalue problem. The approach divides the rotor/beam into segments based on change in diameter and bearing/disc locations. Afterwards, a segment-by-segment buildup is initiated to complete the global mass, stiffness, and Coriolis matrices for the eigenvalue problem. An example problem is modelled and its Campbell diagram is presented.

Chapter 3

Active Magnetic Bearing Topologies and Modelling

This chapter describes the two active magnetic bearing topologies for micro-milling spindles considered in this thesis, along with analytical and finite element method approaches.

3.1 Miniaturized Combined Radial-Axial Bearing

Compared to conventional magnetic bearing configurations with slender rotors, as described in Section 3.2, a considerable reduction in rotor length enables a miniaturized arrangement of radial and axial bearing stators. As explained in Section 1.2, a reduction in rotor slenderness leads to increased flexural (bending) resonances providing the following benefits: **(1)** the spindle can be operated at higher speeds without overlap of operating speed and flexural modes. The forward rigid conical mode is also avoided in the operation range (refer to Section 4.3.1), and **(2)** a higher flexural mode prevents resonance due to machining excitations.

3.1.1 Bearing topology

Adopting a miniaturized bearing arrangement, the combined radial-axial bearing topology adopted from Lee [16] showing the bias and control flux paths is depicted in Fig. 3.1. It consists of a short rotor supported by a permanent magnet (PM)-biased combined radial-axial magnetic bearing. The PM rings with radially inward magnetization provide bias flux for both radial and axial stators. With a relative magnetic permeability almost equal to that of the air, the PM rings almost separate the paths of axial and radial control fluxes. For the axial control of the rotor, the control flux generated by the axial coils travels across the rotor axially. The empty space within the axial stator is kept for motor integration for the future work related to this study. The radial control flux is intended to stay within the radial stators. For the radial stator, a homopolar topology is adopted. In this homopolar arrangement, the rotor segments facing the radial stator do not experience a change in magnetic polarity. This leads to reduced eddy current losses in the rotor, especially in high-speed applications where the centrifugal stresses discourage the use of the laminated rotors. The material selection for all components is justified in Section 4.2.

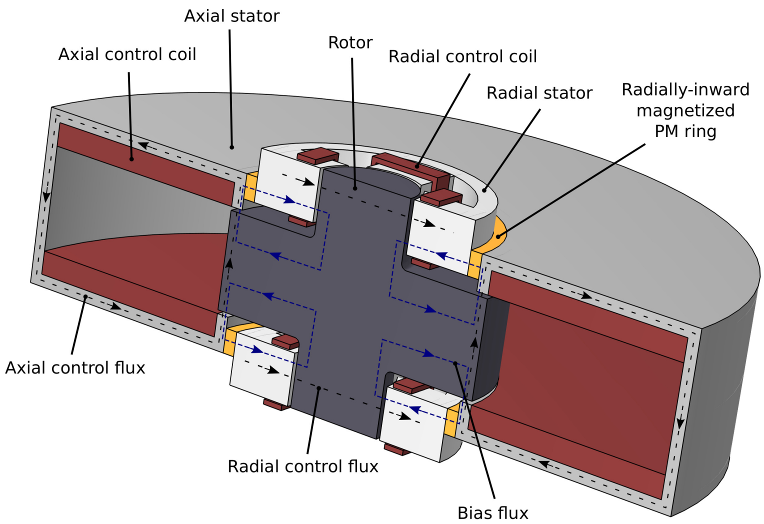

Figure 3.1: Half-section view of the bearing topology showing bias and control flux directions.

3.1.2 Finite element model

We used the *Rotating Machinery, Magnetic (rmm)* interface of COMSOL AC/DC module to develop a three-dimensional (3D) finite element (FE) model of the bearing arrangement to aid the initial design and the optimization process. This interface uses the moving mesh approach to model the rotations and solves Maxwell's equations using a combination of magnetic vector and scalar potentials as dependent variables [40]. In vector potential formulation, the magnetic vector potential $\mathbf{A}$ is linked to magnetic flux density $\mathbf{B}$ and electric field $\mathbf{E}$ as:

$$\mathbf{E} = -\frac{\partial \mathbf{A}}{\partial t} \tag{3.1}$$

$$\mathbf{B} = \nabla \times \mathbf{A} \tag{3.2}$$

These definitions of fields **E** and **B** fulfil the two Maxwell's equations: Faraday's law and magnetic Gauss' law defined in Eqs. (3.3) and (3.4), respectively.

$$\nabla \times \mathbf{E} = -\frac{\partial \mathbf{B}}{\partial t} \tag{3.3}$$

$$\nabla \cdot \mathbf{B} = 0 \tag{3.4}$$

The equation to be solved is Ampere's law, given in Eq. (3.5), which equates the curl of magnetic field intensity **H** to the current density **J**.

$$\nabla \times \mathbf{H} = \mathbf{J} \tag{3.5}$$

In scalar potential formulation, the magnetic field intensity is defined as the gradient of magnetic scalar potential V_m in Eq. (3.6). This results in Ampere's law being automatically fulfilled and afterwards magnetic Gauss' law is solved.

$$\mathbf{H} = -\nabla V_m \tag{3.6}$$

Considering that the magnetic bearing has electrically conductive and non-conductive components, we opted for a *mixed formulation* in COMSOL. Here, the conductive domains are assigned vector potential formulation (implemented by *Ampere's Law* node) and the non-conductive ones are assigned scalar potential formulation (implemented by *Magnetic Flux Conservation* node). All bearing components were divided into rotating and stationary domains, with a boundary cut separating both domains. All the flux carrying components were enclosed in airgap so that flux leakage and fringing effects can be studied. The radial and axial airgaps around the boundary cut were assigned scalar potential formulation, and a *Continuity* pair feature enforced the continuity of electromagnetic field. The constitutive relations in the form of built-in B-H curves were used to include non-linear magnetization and saturation effects in the model. For improved numerical stability, *Gauge Fixing for A-Field* feature was applied on all domains with vector potential formulation. A unique solution for magnetic scalar potential is needed for solver convergence, hence the *Zero Magnetic Scalar Potential* node was applied at a point on each side of the boundary cut. For the linear system solver, multifrontal massively parallel sparse direct solver (MUMPS) was selected. To improve simulation performance, the linear discretization order of FE mesh was selected for both magnetic vector and scalar potential regions. For more accuracy, a relative tolerance of $1\text{x}10^{-5}$ was selected for the nonlinear solver.

Finer tetrahedral elements were used for bearing components, while a less fine mesh was used for the surrounding air region. Refining the mesh further resulted in rotor forces within 0.8% of that obtained from the mesh size used for this study. Thus, the constructed model instilled confidence in the solution accuracy and ensured reasonable solution times in the optimization studies. The mesh depicted in Fig. 3.2 (a) shows the finer elements used for rotating and force calculation domains. Fig. 3.2 (b) is the mesh element quality histogram based on the quality measure of skewness. The horizontal axis has quality ranging between 0.0-1.0, where 0.0 reflects a degenerated element and 1.0 refers to the best possible element; the vertical axis has the number of elements of similar quality. This histogram shows an overall acceptable quality of the mesh, since most of the elements stay in the higher quality range.

More FE model details relating to the optimization objective functions are given in Section 4.4.1.

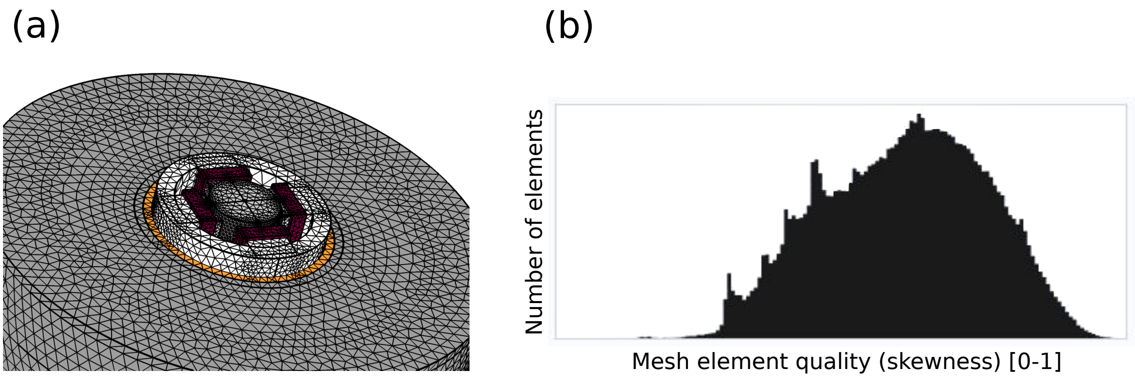

Figure 3.2: (a) Tetrahedral mesh with finer elements at force calculation domains, (b) element quality histogram based on skewness

3.2 Conventional Magnetic Bearings

In many applications, separate radial and axial magnetic bearings are used. Such configurations are easier to manufacture and control system design is simpler when compared with miniaturized combined bearing configurations. In this section, we present radial and axial bearing models based on the finite element method.

3.2.1 Radial bearing

Similarly to the combined bearing arrangement, a PM-biased homopolar topology is selected for radial bearing. In this arrangement, the rotor segments facing the bearing do not experience a change in magnetic polarity. This leads to reduced eddy current losses in the rotor, especially in high-speed applications where the centrifugal stresses discourage the use of the laminated rotors. The bearing topology is presented in Fig. 3.3 with dashed lines showing the magnetic flux paths. Two stators have eight poles in total; four for each stator. Four PMs are used to provide the bias flux. The control coils, excited with current from amplifier, provide the control flux. Observing the directions of both fluxes (bias and control), we notice that on one side of the rotor, the fluxes will be added leading to a higher attractive force compared to the other side where the fluxes will be subtracted. In this way, varying the direction of the control flux through control action can change the direction of the net force acting on the rotor to achieve stable levitation. The control flux travels within the stator and radially in and out of the rotor. The connection between PMs and stator was made by connectors having a good magnetic performance. The non-magnetic housings were used to hold the assembly together.

The development of the finite element method is treated next.

3.2.1.1 Finite element model

The 3D FE model used for for this radial bearing uses the same COMSOL AC/DC module and *rmm* interface from Section 3.1.2. The assignment of the domains to scalar potential and vector potential formulations was done in the same manner as done for the miniaturized combined bearing. Therefore, only mesh details are discussed in this section.

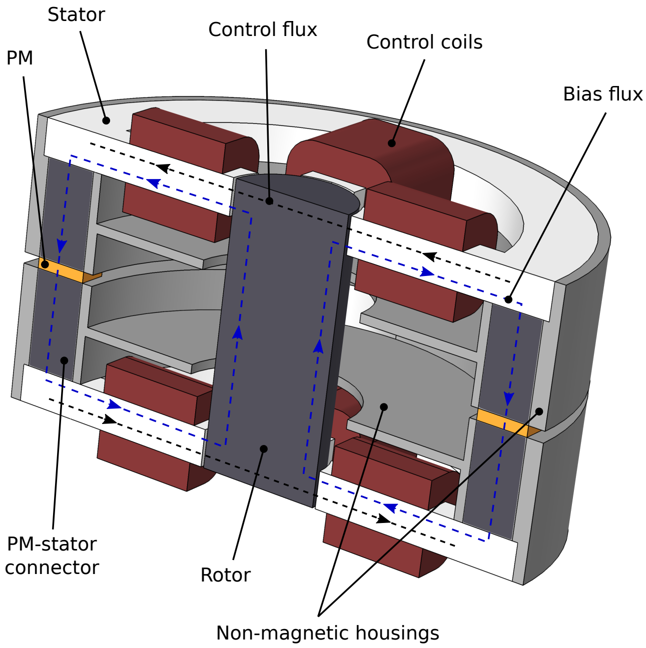

Figure 3.3: Half-section view of the radial bearing topology with bias and control flux directions in dashed lines.

As done before with miniaturized combined topology, finer tetrahedral elements were used for bearing components, while a less fine mesh was used for the surrounding air region. Refining the mesh further resulted in rotor forces within 0.8-1.0% of that obtained from the mesh size used for this study. This led to confidence in the solution accuracy and ensured reasonable solution time. The mesh shown in Fig. 3.4 (a) contains finer elements used for rotating and force calculation domains. Fig. 3.4 (b) is the mesh element quality histogram based on the quality measure of skewness. The horizontal axis has quality ranging between 0.0-1.0, where 0.0 reflects a degenerated element and 1.0 refers to the best possible element; the vertical axis has the number of elements of similar quality. This histogram shows an overall acceptable quality of the mesh, since most of the elements stay in the higher quality range.

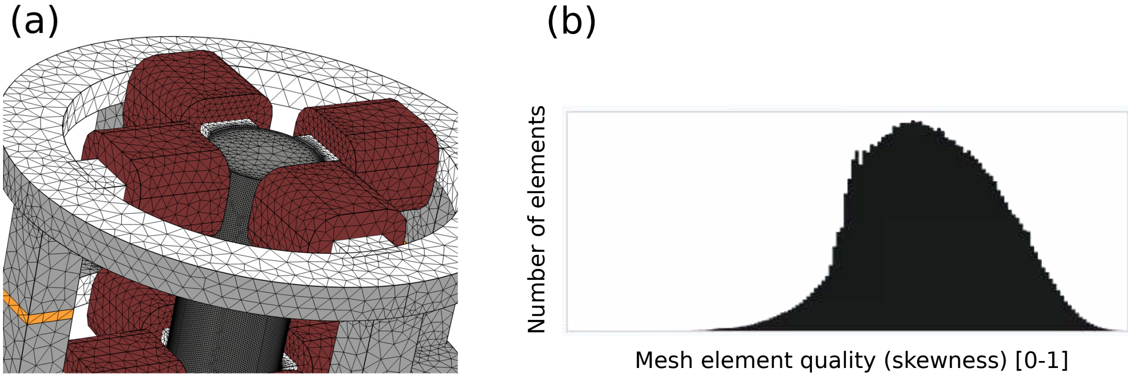

Figure 3.4: (a) Tetrahedral mesh with finer elements for force calculation domains, (b) Element quality histogram based on quality measure of skewness

3.2.2 Axial thrust bearing

The derivation of thrust bearing force is treated in this section to dimension the bearing. The force generated in a reluctance actuator is given by:

$$f_{\mathrm{R}} = \frac{\mu_{\mathrm{o}} n^2 A_{\mathrm{p}} i^2}{4 l_{\mathrm{a}}^2} \tag{3.7}$$

where μ_{o} is the relative permeability of air, n is the number of winding turns, A_{p} is the area of each pole, i is the current, and l_{a} is airgap length. For a detailed derivation of the reluctance force, the reader is referred to Kimman [15].

Since the electromagnetic actuators generate an attractive force, a second actuator, positioned opposite to the first, is needed for levitation control and compensation of external forces. Such can be called a double-sided configuration. We assume n and A_p are same for both actuators, l_{a1} is the airgap length between rotor and actuator 1, l_{a2} is the airgap length between rotor and actuator 2, and i_1 and i_2 are the winding currents in actuators 1 and 2, respectively. The net force F can be written as:

$$F = f_{\mathrm{R1}} - f_{\mathrm{R2}} = \frac{\mu_{\mathrm{o}} n^2 A_{\mathrm{p}}}{4} \left(\frac{i_1^2}{l_{\mathrm{a1}}^2} - \frac{i_2^2}{l_{\mathrm{a2}}^2} \right) \tag{3.8}$$

As noticed in Eq. (3.8), the dependence of reluctance force on currents and airgap lengths is nonlinear. Particularly, the quadratic dependence of force on current leads to a low force slew rate (rate of change of actuator force) when the coils are not excited by any current [41]. To linearize this relation between force and current, the winding current are divided into two components, namely bias current i_b and perturbation current i_p. One of the actuation methods for a double-sided configuration is the differential driving mode where the perturbation current is added to bias current in one actuator and subtracted in the other actuator. The current in both actuators are given by:

$$i_1 = i_\mathrm{b} + i_\mathrm{p} \tag{3.9}$$

$$i_2 = i_\mathrm{b} - i_\mathrm{p} \tag{3.10}$$

With the condition that perturbation current does not exceed the bias current. Assuming the rotor is placed at an equal airgap length from both actuators, *i.e.* $l_\mathrm{a1} = l_\mathrm{a2} = l_\mathrm{a}$, Eq. (3.8) becomes:

$$F = \frac{\mu_\mathrm{o} n^2 A_\mathrm{p}}{l_\mathrm{a}}\, i_\mathrm{b} i_\mathrm{p} \tag{3.11}$$

It can be noticed that the net force acting on the rotor is now proportional to the perturbation current i_p while the bias current i_b is kept constant. The introduction of bias field also increases the force slew rate. During the operation, the nominal airgap lengths also change as rotor displaces from its initial position. Taking z as the rotor displacement, we define the actual airgap lengths for two actuators as:

$$l_\mathrm{a1} = l_\mathrm{o} - z \tag{3.12}$$

$$l_\mathrm{a2} = l_\mathrm{o} + z \tag{3.13}$$

Substituting the relations for currents and actual airgap lengths in Eq. (3.8), the net force is given by:

$$F = \frac{\mu_\mathrm{o} n^2 A_\mathrm{p}}{4} \left(\frac{(i_\mathrm{b} + i_\mathrm{p})^2}{(l_\mathrm{o} - z)^2} - \frac{(i_\mathrm{b} - i_\mathrm{p})^2}{(l_\mathrm{o} + z)^2} \right) \tag{3.14}$$

For the application of linear control theory, this force is linearised at the working point [41]. A small perturbation current around the bias current and nominal rotor position (x=0) can be taken as the working point. Next, we expand the Taylor series around the point (x,i_p) = (0,0) and neglect the second and higher order terms to get the linearized net force as:

$$F = \frac{\mu_{\rm o} n^2 A_{\rm p} i_{\rm b}}{l_{\rm o}^2}\, i_{\rm p} + \frac{\mu_{\rm o} n^2 A_{\rm p} i_{\rm b}^2}{l_{\rm o}^3}\, z \tag{3.15}$$

$$F = K_{\rm i} i_{\rm p} + K_{\rm z} z \tag{3.16}$$

where K_i is known as force-current dependency or (open loop current gain) and K_z is known as force-displacement dependency (or open loop stiffness or negative stiffness) of AMB actuator.

3.3 Summary and Recommendations

This chapter has discussed two topologies for active magnetic bearings and developed the finite element (FE) models of these topologies. First, the miniaturized combined radial-axial bearing is described and then an FE model is discussed. Similarly, the conventional magnetic bearings are treated. A finer mesh is utilized in the force calculation domains. The presented histograms show an overall acceptable quality of mesh. The axial thrust bearing is simply modelled using the force relations of double-sided reluctance actuators driven in a differential mode. One recommendation regarding the future work is:

- In most cases, the axial bearings are biased by coil current. However, recent literature shows promise of using permanent magnets to provide bias flux. Such an arrangement has resulted in significant improvements in the actuator bandwidth [42].

Chapter 4

Miniaturized Spindle Design and Optimization

This chapter describes the design and FE-based multiobjective optimization of the miniaturized spindle modelled in Section 3.1. The topology is depicted in Fig. 4.1. The initial design is based on the micro-milling application requirements and developed using the FE model. The material selection is influenced by application and reasonable availability of materials in the local market. Gradient and nongradient-based optimization methods were used to minimize single and weighted-sum multiobjective functions.

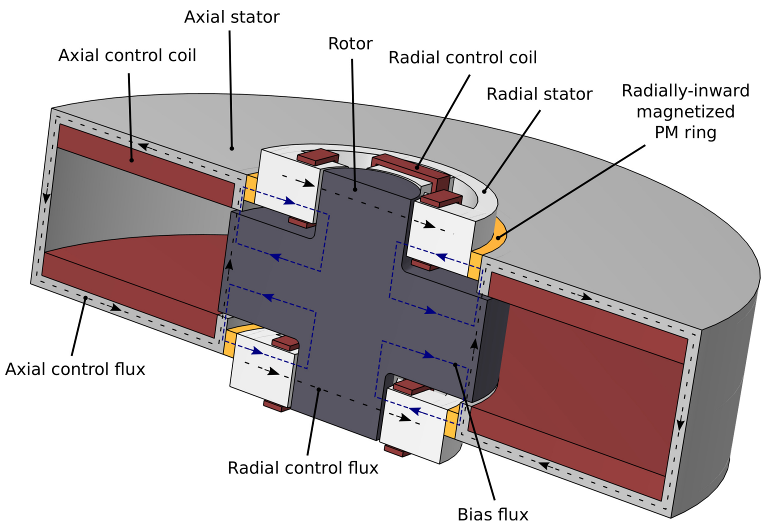

Figure 4.1: Half-section view of the bearing topology showing bias and control flux directions.

4.1 Application Requirements

The miniaturized combined radial-axial magnetic bearing shown in Fig. 4.1 is aimed at high-speed milling operation, which influences the component design. Due to the process dynamics and control systems, there are several requirements in terms of rotational speed, milling forces, and negative stiffness.

4.1.1 Rotational speed

In a nutshell, micro-milling is the scaled-down version of macro-scale (conventional) mechanical milling. However, the small diameter (micro-scale cutting) tools, that can go down to 50 μm in diameter, used in micro-milling reduce the chip removal rate. Therefore, to achieve process efficiency (*i.e.*, to attain high material removal rates), cutting tools need to rotate at high rotational speeds [11]. For this purpose, miniature ultra-high-speed (UHS) spindles which enable rotational speeds above 60,000 rpm are used in micro machine tools (μMT) [1, 10].

In this study, we assumed a typical micro-milling tool diameter of 200 μm and a typical cutting speed of 130 m.min^{-1} which is sufficient for the machining of various common materials. In theory, this requires a rotational speed of 206,900 rpm. Therefore, we set the target speed as 207,000 rpm (3450 Hz).

4.1.2 Milling forces

Another important requirement is the (milling or cutting) forces experienced by the bearings. The milling forces depend on the cutting mechanics and determined based on the machining conditions (such as depth of cut, feed rate, spindle speed, etc.) and tool geometry [1].

To estimate the amplitude of micro-milling cutting forces, the model proposed by Dow *et al.* [43] is used. Using this model, Kimman *et al.* [9] performed a slot milling process with a 200 μm cutting tool. The feed rate of 5 μm per tooth and the depth of cut of 5 μm were selected. Considering a vertical milling operation, the static components of cutting forces were obtained as 0.08 N and 0.05 N along lateral axes. Furthermore, a slightly higher static component of 0.5 N along the axial axis was found. The dynamic force amplitude stayed around 0.3 N in all directions.

While the static components of cutting forces can be compensated by AMBs, the bandwidth limit makes the dynamic force compensation challenging.

4.1.3 Negative stiffness

Considering the milling forces described above, a controlled closed-loop bearing stiffness of 1.4×10^5 N/m is desired to compensate for the static cutting forces [15]. As a rule of thumb, a negative bearing stiffness of the same magnitude, or at most one order of magnitude lower, can be selected [41]. Therefore, the negative stiffness is limited between 1×10^4 - 1×10^5 N/m in this study.

4.2 Material Selection

Considering the future realization of the designed spindle, the material selection is influenced by reasonable availability of materials and the application requirements. Thus, for magnetic actuators, in addition to laminated electrical steel, ferritic stainless steels (SS) with soft magnetic properties (typical intrinsic coercivity of less than 1000 Am^{-1}) are generally used. However, ferritic SS have lower mechanical strength limiting the achievable rotational speeds.

In practice, the solid rotor segments facing radial bearing stators are press-fitted with electrical steel laminations which reduce eddy current and hysteresis losses; and exhibit a low coercivity and high magnetic permeability [44]. However, ultra-high speeds result in centrifugal stresses which may disturb this press-fit, justifying the use of a complete solid rotor. Trading off between magnetic properties and mechanical strength, we selected a ferritic SS of annealed AISI 430F for the rotor.

Since the axial magnetic bearing geometry makes the construction from electrical steel laminations almost impractical [45], we used the solid core of AISI 430F for the axial stator. AISI 430F provides good magnetic performance and easy machinability. In the case of radial stator, laminated electrical steel with high magnetic performance (as aforementioned) was selected.

Lastly, we selected sintered neodymium-iron-boron (NdFeB) magnets for PM rings. The sintered grades favour high remanence and coercivity. It should be noted that NdFeB magnets undergo limited loss in remanence but a significant loss in coercivity when heated to temperatures above 100 °C [46]. While substitution of dysprosium and cobalt for some part of the neodymium helps raise the coercivity and reduce the Curie temperature, respectively; such substitutions may negatively affect other properties desirable for our soft magnetic application. For example, the addition of dysprosium leads to a decrease in the remanence [47]. To keep the temperature in control in the absence of forced cooling in the bearing topologies studied in this thesis, we limited the coil current densities within the recommended range of 2-5 A/mm^2 [48]. Since the topology in this chapter positions the permanent magnet away from the current coils, we do not expect the temperatures to significantly rise.

4.3 Component Design

The 3D FE model developed in Section 3.1 is used for the analysis and the magnetic bearing components are dimensioned based on the application requirements (see Section 4.1).

4.3.1 Rotor

A high-speed rotation leads to significant stresses under centrifugal forces, which limit the attainable rotational speed Ω_{max}. The maximum rotational speed Ω_{max} can be related to the disc diameter as

$$\Omega_{max} = \frac{1}{r}\sqrt{\frac{8\sigma_o}{(\nu+3)\rho}} \tag{4.1}$$

where r is the radius of the disc, σ_o is the yield strength, ν is the Poisson's ratio, and ρ is the density of the rotor material [44]. Using annealed AISI 430F as rotor material with σ_o = 275 MPa, ν = 0.27, and ρ = 7750 kg/m^3, a maximum disc diameter of 27.2 mm is obtained for a rotational speed of 207,000 rpm. Rotor diameter is kept at 8 mm to attach end mills with typical micromachining tool shank diameters. The axial length of the rotor disc is taken from Borisavljevic *et al.* [49] to allow future attachment of PM rings for a motorized spindle. Next, the overall length of the rotor is decided based on the axial length of radial stators and coils (described in the next subsection).

With the initial dimensions fixed and shown in Table 4.1, we performed a rotor dynamic analysis of rotor. The first flexural resonance is aimed to be at least one order of magnitude higher than the aimed closed-loop actuator bandwidth of 300 Hz [9]. Additionally, our rotational speed requirement of the rotor stands at 3450 Hz (207,000 rpm). We used an existing in-house MATLAB rotor dynamic code [39] enhanced with the spectral Chebyshev approach [17, 27] to develop the Campbell diagram of the rotor as shown in Fig. 4.2. Based on the rotordynamic simulation, it is observed that not only the first flexural mode, predicted as 36180 Hz, is significantly higher than the rotational speed requirement, but also the forward rigid conical mode is avoided as it diverges from the synchronous excitation line. A half-section view of the rotor is shown in Fig. 4.3 (a).

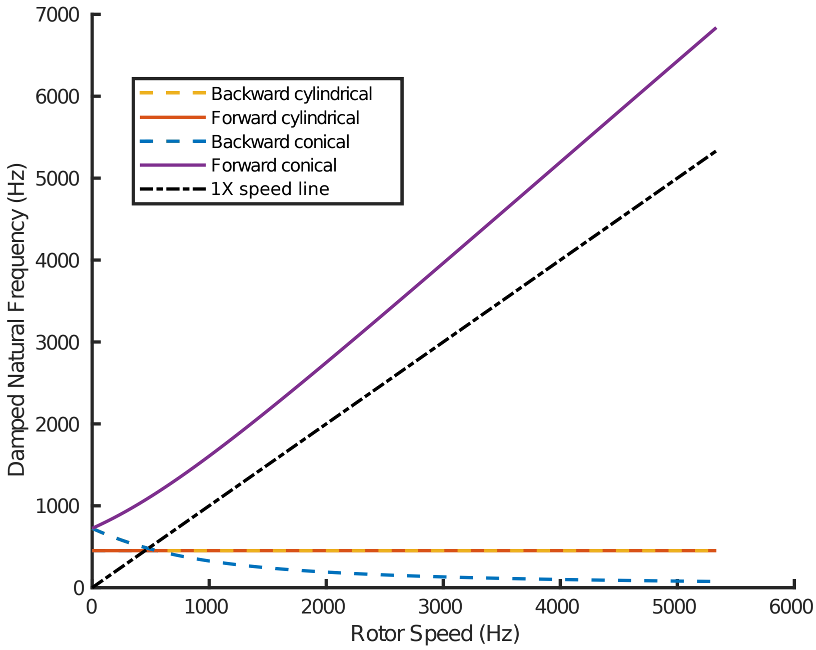

Figure 4.2: Rotor Campbell diagram showing the variation of first four damped rigid body modes with the rotational speed.

4.3.2 Radial magnetic stator

To radially control the rotor levitation, two radial stators, each having four poles were used as shown in Fig. 4.1. Since magnetic materials undergo nonlinear magnetization in response to the applied magnetic field, it is advisable to operate in the linear range of material B-H curves. This enables the applied coil current and the control force to become linearly dependent on each other. The B-H curves of stator and rotor materials, laminated electrical steel and AISI 430F, respectively, are almost linear up to 1 T. As a rule of thumb, the bias flux level is kept at half of this value, *i.e.* 0.5 T [34].

Considering a well-balanced rotor and accounting for the backup bearing, a radial air gap of 0.3 mm is selected. The NdFeB grade N28 PM ring is dimensioned to provide around 0.5 T of bias flux levels in the air gap. Although the radial cutting forces on the tool are limited to a static component of 0.08 N and a dynamic amplitude of almost 0.3 N as discussed in Section 4.1, we set the lowest bearing radial load capacity as 2 N accounting for unbalance and possible disturbances. Furthermore, radial negative stiffness between $1 \text{x} 10^4$ and $1 \text{x} 10^5$ Nm^{-1} needs to be ensured. To achieve these goals, we manually iterate the stator pole area, coil turns, and applied current. Accordingly, the initial dimensions and key parameters of the radial stator are listed in Table 4.1 and a half-section view is shown in Fig. 4.3 (b).

4.3.3 Axial magnetic stator

The axial stator is dimensioned similar to the radial stator, but it accounts for the rotor weight as well. In response to axial static machining force of 0.5 N and maximum rotor weight of 0.503 N (taking bounds for the maximum weight from Table 4.2), we set a sufficiently high bearing axial load capacity of 5 N as lowest acceptable value. The stator supports the rotor axially by electromagnetic forces from two circular-ring poles as shown in Fig. 4.3 (c). The axial air gap length is kept the same as that of radial stators, *i.e.,* 0.3 mm. Another consideration is the space left within the stator for integrating a motor as prototyped by Borisavljevic [50]. The dimensions of the axial stator are given in Table 4.1.

4.3.4 Conductor coils

In most naturally cooled motor and magnetic bearing applications, copper coil current densities between 2-5 A/mm^2 are recommended [48]. Using current density of 5 A/mm^2 and a maximum coil current of 0.5 A, we get a recommended wire diameter of 0.36 mm which very closely is found in American Wire Gauge (AWG) 27 wire.

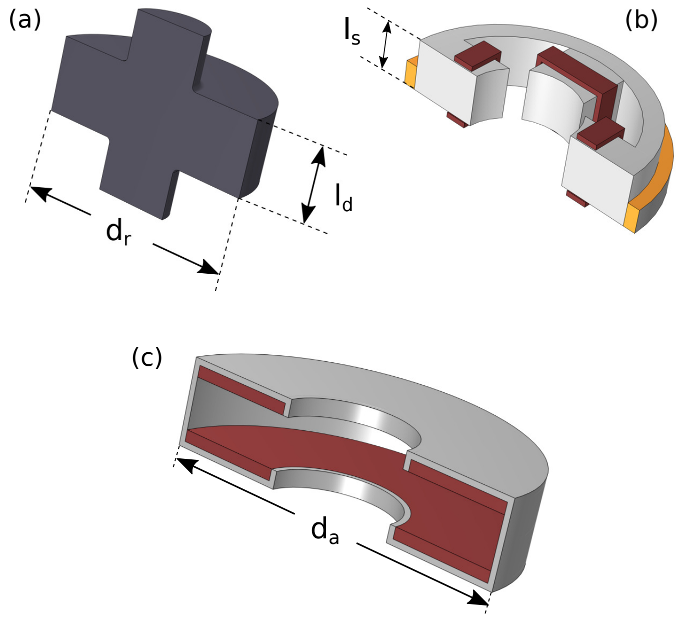

Figure 4.3: Half-section views of AMB components with design variables (a) Rotor, (b) Radial stator with PM, (c) Axial stator

4.3.5 Initial flux density levels

To ensure that the magnetic flux density norm levels did not exceed the linear range of BH curves (1 T), the flux density is plotted using FE model on two planes intersecting different sections of the bearing. As noticed in Figs. 4.4 and 4.5, the flux levels slightly exceed 1 T in very limited regions of the geometry.

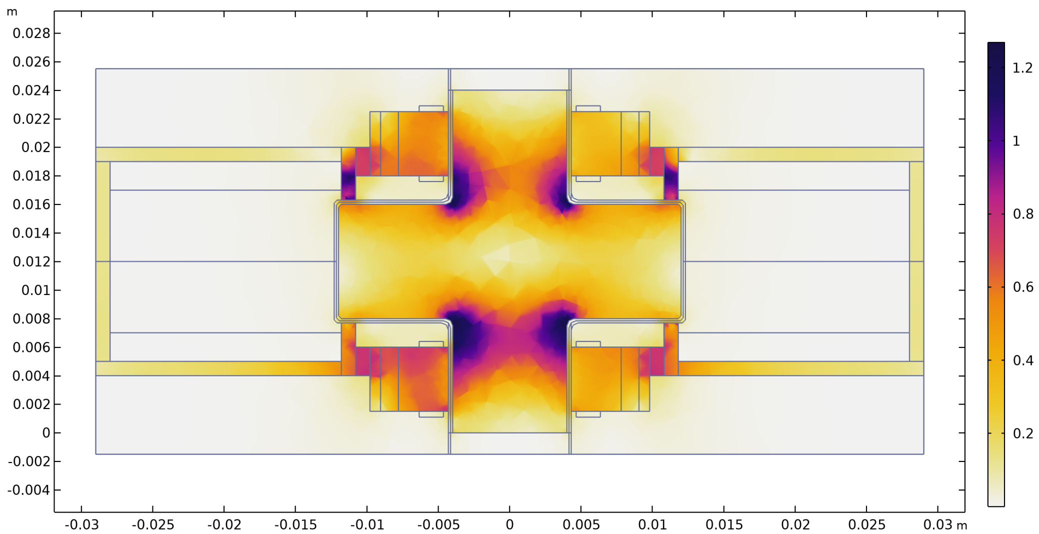

Figure 4.4: Cut plane with magnetic flux density norm passing through half of the bearing topology (compare with Fig. 4.1 for component definition).

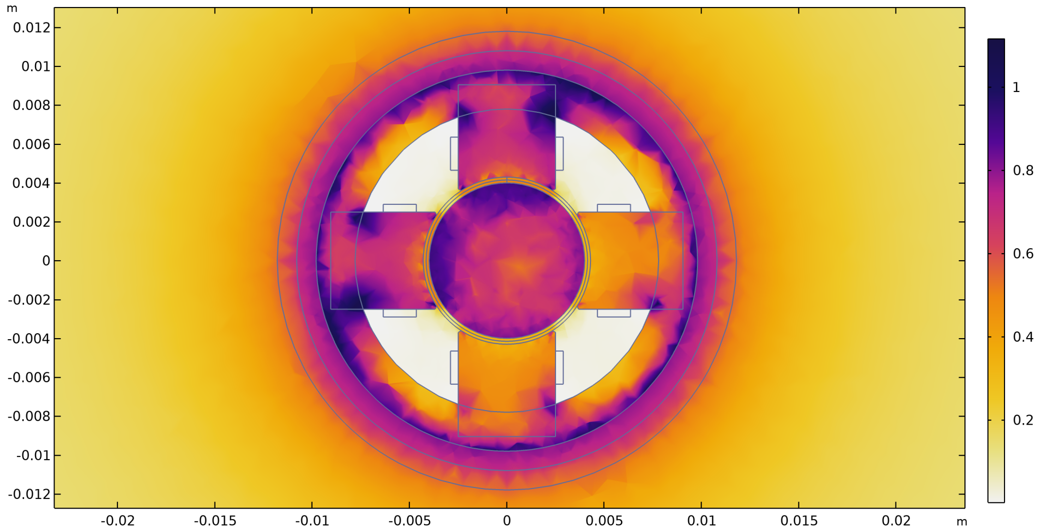

Figure 4.5: Surface magnetic flux density norm on cut plane perpendicular to rotational axis. The plane is positioned to pass through all the components.

Table 4.1: Major AMB parameters

Parameters	**Initial values**
Rotor diameter (mm)	8
Rotor disc diameter (mm)	24
Rotor disc axial length (mm)	8
Rotor length (mm)	24
Radial stator pole area (m^2)	2.29x10^{-5}
Radial stator axial length (mm)	4.5
Radial coil turns per pole	40
Radial coil current (A)	0.5
Axial stator pole area (m^2)	7.1x10^{-5}
Axial stator diameter (mm)	29
Axial coil current (A)	1
Axial coil turns per pole	30
PM inner surface area (m^2)	12.3x10^{-5}

4.4 Optimization Setup

With micro-machining in focus, the selection of objective functions, design variables, and constraints is justified in this section. Next, the implementation of COMSOL-

MATLAB LiveLink™ to run the optimization process is explained.

4.4.1 Objective functions

Specific load capacity is the ratio of the maximum electromagnetic force that the bearing can produce to its volume [14]. With spindle miniaturization and attachment to motorized linear translation stages in mind, a high specific load capacity is desired as the selected bearing performance for optimization. At lower volume, hence lower weight, the spindle can utilize cost-effective linear stages to reach process-required accelerations. The 3D FE model developed in Section 3.1 quantifies this performance by evaluating the bearing forces and component volumes.

The electromagnetic forces acting on the rotor in radial and axial directions are determined by using the general method of Maxwell's stress tensor. To obtain the force, Eq. (4.2) is integrated over the surface of the rotor [40].

$$\mathbf{n}_{\mathrm{r}}\, T_{\mathrm{a}} = -\frac{1}{2}\,\mathbf{n}_{\mathrm{r}}\,(\mathbf{H}\cdot\mathbf{B}) + (\mathbf{n}_{\mathrm{r}}\cdot\mathbf{H})\,\mathbf{B}^{T} \tag{4.2}$$

where $\mathbf{n}_{\mathrm{r}}$ is the outward normal from rotor (r), T_{a} the stress tensor in surrounding air (a), $\mathbf{H}$ the magnetic field, and $\mathbf{B}$ the magnetic flux density. We denote the radial and axial forces as f_{r} and f_{a}, respectively.

An integration nonlocal coupling is used to determine the volumes in COMSOL. The total bearing volume V is the sum of volumes of rotor, V_{r}, PM, V_{pm}, radial stators, V_{rs}, and axial stator, V_{as} as shown in Eq. (4.3).

$$V = V_{\mathrm{r}} + V_{\mathrm{pm}} + V_{\mathrm{rs}} + V_{\mathrm{as}} \tag{4.3}$$

4.4.2 Sensitivity study and design variables

While analytical models enable an easier understanding of the relative importance of various design parameters on bearing performance, an FE model necessitates a sensitivity study since the explicit relations are not evident. This need is further reinforced in compact bearing designs where axial and radial control fluxes affect each other in the presence of non-linear magnetization and saturation effects. We performed a sensitivity study to determine the most effective dimensional parameters for our objective functions.

We perturbed the initial bearing parameters given in Table 4.1 and noted the corresponding variations in radial and axial forces. Based on the sensitivities and preferences based on spindle miniaturization, the parameters tabulated in Table 4.2 and drawn on Fig. 4.3 are selected as design variables. The variables are reasonably bounded by rotordynamic considerations of the short rotor as described in Section 4.3.1.

4.4.3 Size constraints

In addition to the consideration of miniaturization, the size constraints are influenced by rotordynamics, stress limits, and space for motor integration. The size constraints on the rotor disc diameter and length ensure that the forward rigid conical mode of the rotor remains divergent as the rotor speeds up as shown in Fig. 4.2. The disc diameter is also limited by maximum allowable value calculated in Section 4.3.1. The constraints ensure a ratio of polar and transverse moments of inertia greater than 1.18 and the first flexural mode remains significantly farther from the operating speed range.

The size constraints for the radial stator axial length are based on the available rotor length. The radius of the axial stator is ranged considering the required space for motor integration and the overall spindle size. All the side constraints are given in Table 4.2.

Table 4.2: Design variables with initial and limiting values

Design variables	**Symbols**	**Initial values (mm)**	**Lower bounds (mm)**	**Upper bounds (mm)**
Radial stator axial length	l_{s}	4.5	3	6
Rotor disc diameter	d_{r}	24	23.6	27.2
Axial stator diameter	d_{a}	58	50	58
Rotor disc length	l_{d}	8	7	10

4.4.4 COMSOL LiveLink^{TM} for MATLAB setup

Using the COMSOL LiveLink^{TM} for MATLAB, the FE model developed in COMSOL was interfaced with MATLAB. The optimization algorithm was run within MATLAB. This subsection summarizes this interfacing. After running *COMSOL Multiphysics with MATLAB* from the installation directory, three MATLAB files can be written:

1. Main script file to define the design variables, load FE model file, and set up optimization algorithm settings.
2. Function file to receive updated design variables, run the FE model in COMSOL with updated design variables, and pass the retrieved objective function values to main script file.
3. Function file which contains the constraints.

The codes written for multiobjective optimization are given in Appendix A with comments explaining step-by-step procedure.

4.5 Optimization Results

The objective functions were first optimized individually using single-objective optimizations (SOO). When one objective was minimized in SOO, the other two worked as unequal constraints from engineering demand, *i.e.* $f_r \geq 2$ N and $f_a \geq 5$ N. This allowed us to calculate the weighting coefficients for the weighted sum function in multi-objective optimization (MOO) where three objectives were linearly superposed. Considering the nonlinear optimization problem at hand with bound constraints, the gradient-based optimization algorithm of Sequential Quadratic Programming (SQP) was adopted first. SQP is considered as state of the art in nonlinear programming methods. Considering that gradient-based methods are local optimization methods, we also opted for a global (nongradient) method of surrogate optimization. Although the objective functions of forces need to be maximized, we treated them with a negative sign in SOO so that all objective functions meet the definition of minimization.

4.5.1 Single-objective optimizations

Using the initial values and bound constraints from Table 4.2, the first objective function of radial force f_r is optimized first. The convergence is shown in Fig. 4.6 with design variables optimized to:

$$[\,l_\mathrm{s} \;\; d_\mathrm{r} \;\; d_\mathrm{a} \;\; l_\mathrm{d}\,]^\mathrm{T} = [\,5.88 \;\; 27.19 \;\; 50 \;\; 9.99\,]^\mathrm{T} \;\; \mathrm{mm} \tag{4.4}$$

The initial and SOO values are shown in Table 4.3. We also ran a brute force search between bounds for l_s while keeping all other design variables at their optimized values. As seen in Fig. 4.7 and more refined function evaluations in Fig. 4.8, the optimized point (force) is very close to the minimum of the brute force curve. In all the plots in this chapter, the circles show the points where the functions were evaluated.

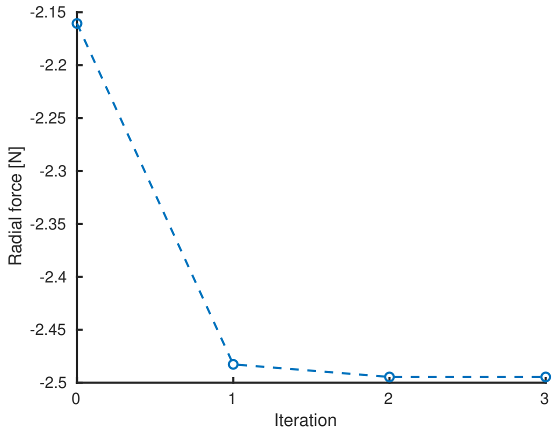

Figure 4.6: Radial force optimization iterations

Similarly, the **second objective function** of axial force f_a is optimized. The convergence is shown in Fig. 4.9 with design variables optimized to:

$$[\,l_\mathrm{s} \;\; d_\mathrm{r} \;\; d_\mathrm{a} \;\; l_\mathrm{d}\,]^\mathrm{T} = [\,6 \;\; 25.38 \;\; 50.03 \;\; 7\,]^\mathrm{T} \;\; \mathrm{mm} \tag{4.5}$$

The initial and SOO values are shown in Table 4.3. A brute force search was also run between bounds for d_r with all other design variables at their optimized values. As seen in Fig. 4.10, the optimized point (force) is very close to the minimum of the brute force curve.

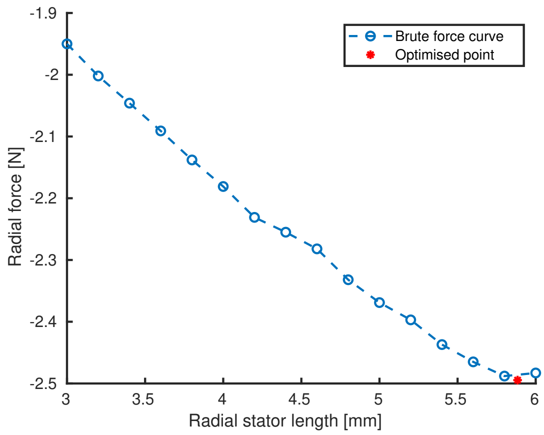

Figure 4.7: Variation of radial force as a function of axial stator diameter.

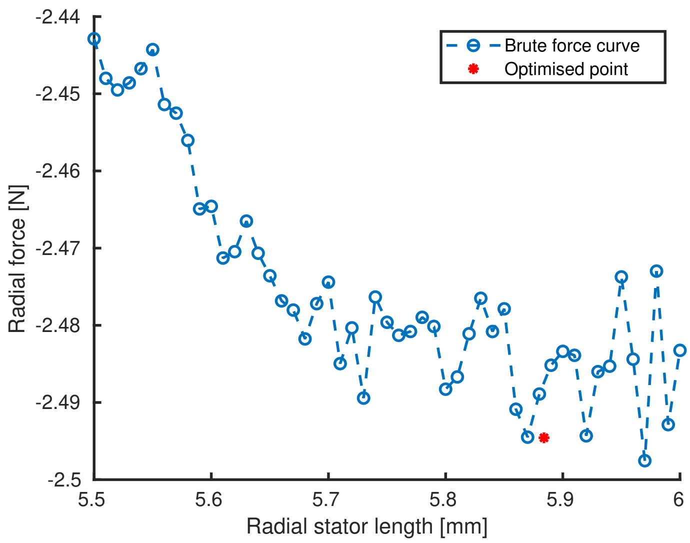

Figure 4.8: More refined function evaluations showing variation of radial force as a function of axial stator diameter.

The optimization of the **third objective function** of volume V is straight forward. All design variables will hit the lower bounds to reduce the volume:

$$[\, l_\mathrm{s} \;\; d_\mathrm{r} \;\; d_\mathrm{a} \;\; l_\mathrm{d} \,]^\mathrm{T} = [\, 3 \;\; 23.6 \;\; 50 \;\; 7 \,]^\mathrm{T} \;\; \mathrm{mm} \tag{4.6}$$

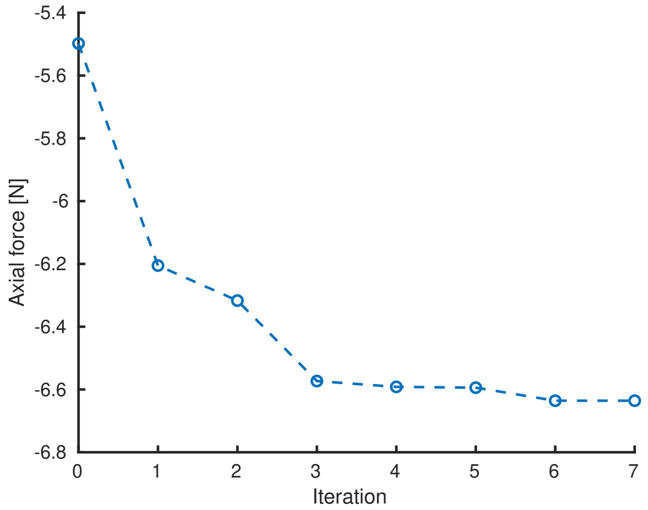

Figure 4.9: Axial force optimization iterations

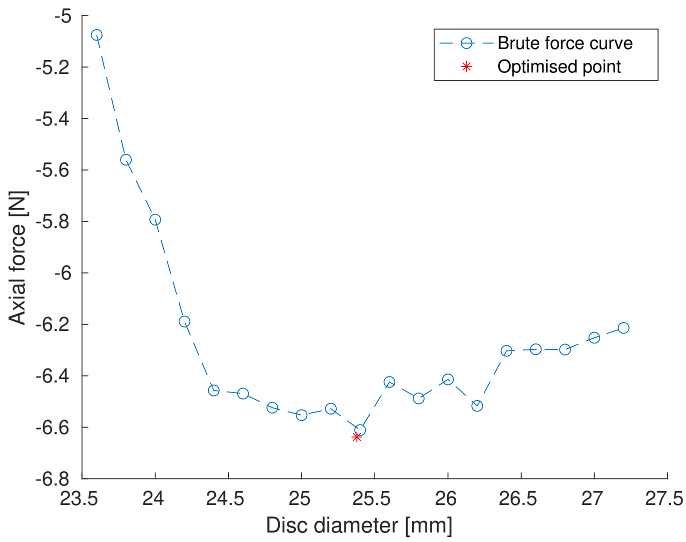

Figure 4.10: Variation of axial force as a function of disc diameter.

To have increased confidence in the optimization, the radial and axial forces were also optimized using **surrogate optimization method**. As noted in Fig. 4.11, the radial force is maximized to 2.48757 N, very close in comparison to radial force SQP optimization of 2.4846 N. The final design variables from the surrogate optimization are

$$[\, l_\mathrm{s} \quad d_\mathrm{r} \quad d_\mathrm{a} \quad l_\mathrm{d} \,]^\mathrm{T} = [\, 5.88 \quad 26.7 \quad 57.68 \quad 9.69 \,]^\mathrm{T} \quad \mathrm{mm} \tag{4.7}$$

A significant difference in axial stator diameter between SQP and surrogate optimization results can be explained by running a brute force search between bounds. Such a search results in an almost oscillatory behavior of the radial force. Hence, it can be concluded that the radial force is not sensitive to variations in the axial stator diameter.

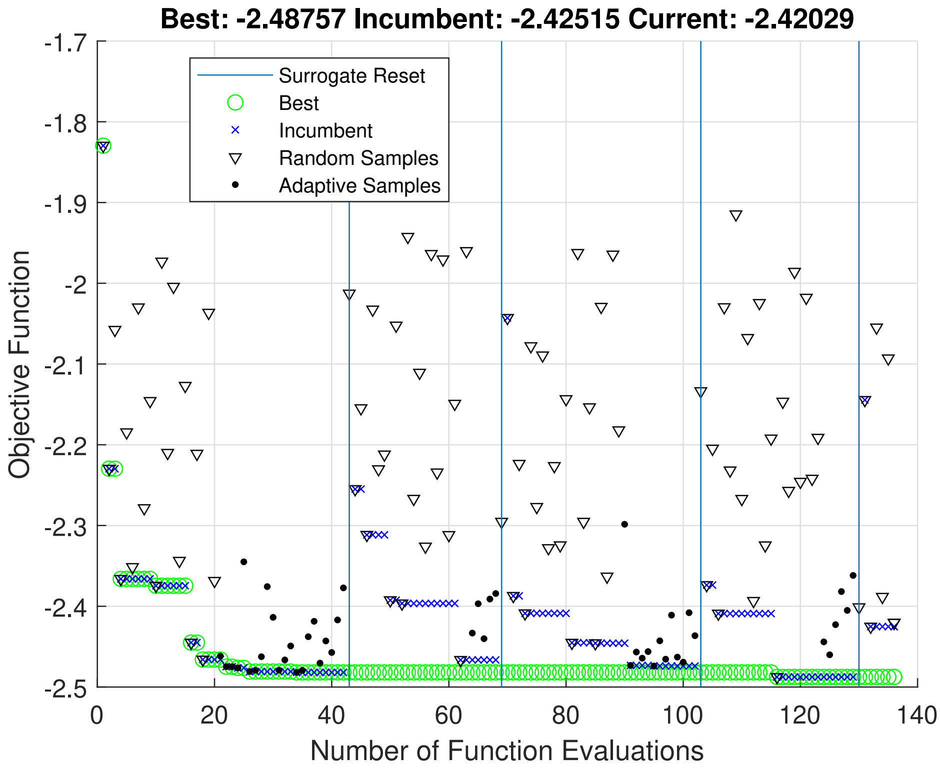

Figure 4.11: Surrogate optimization for radial force.

Similarly, a surrogate optimization for axial force was run and the iterations are shown in Fig. 4.12. The axial force is optimized to 6.50458 N as opposed to SQP optimization of 6.6378 N. The final design variables from the surrogate optimization are given below and are very close to the ones found from SQP optimization.

$$[\, l_\mathrm{s} \quad d_\mathrm{r} \quad d_\mathrm{a} \quad l_\mathrm{d} \,]^\mathrm{T} = [\, 6 \quad 25.37 \quad 50.3 \quad 7 \,]^\mathrm{T} \quad \mathrm{mm} \tag{4.8}$$

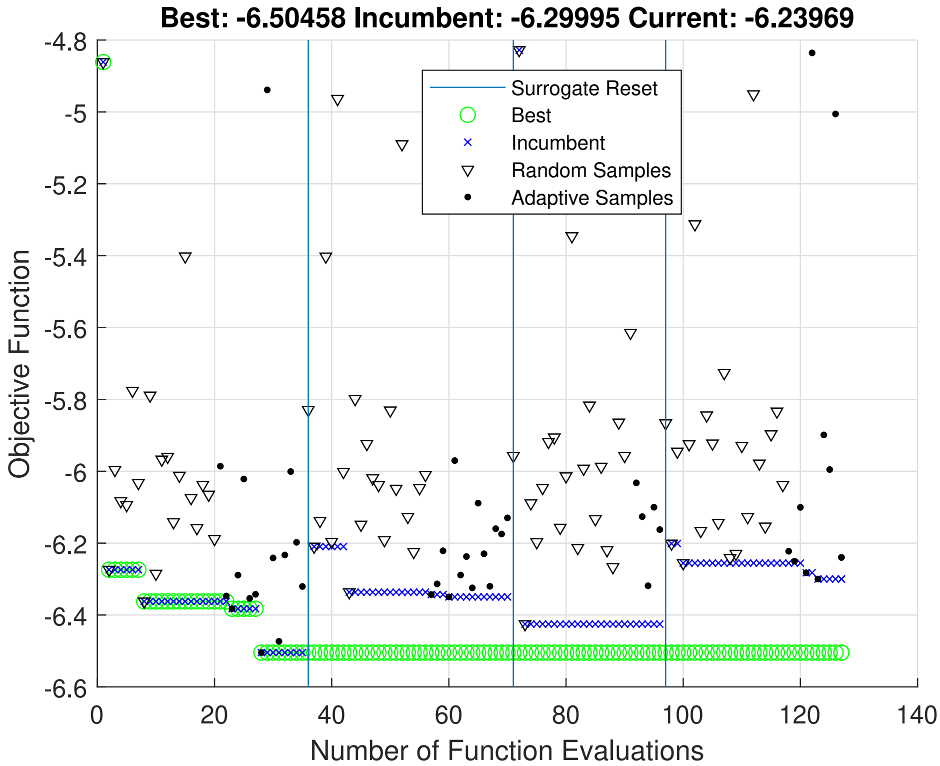

Figure 4.12: Surrogate optimization for axial force.

4.5.2 Multi-objective optimization

With SOO results, we calculated the weighting coefficients for the weighted sum function to optimize the multiobjective problem. The optimization rates r_i for SOO are calculated as

$$r_i = \left| \frac{f_i - f_i'}{f_i} \right| \tag{4.9}$$

where $i = 1, 2, 3$, f_i is the initial objective value, and f_i' is the optimized objective of SOO. Next, we get the normalized optimization rates $w_{\text{norm},i}$ by:

$$w_{\text{norm},i} = \frac{r_i}{\sum_{i=1}^{3} r_i} \tag{4.10}$$

Since we are dealing with objectives with different units and orders of magnitude, non-dimensionalizing (ND) coefficients $w_{\mathrm{nd},i}$ are introduced as:

$$w_{\mathrm{nd},i} = \begin{cases} f_i' & \text{for objectives to be maximized} \\ \frac{1}{f_i'} & \text{for objectives to be minimized} \end{cases} \tag{4.11}$$

Now, the weighting coefficients w_i can be written as following:

$$w_i = w_{\mathrm{norm},i} \; w_{\mathrm{nd},i} \tag{4.12}$$

This allows us to write the weighted sum multiobjective optimization (MOO) function F in Eq. (4.13).

$$F = w_1 \frac{1}{f_\mathrm{r}} + w_2 \frac{1}{f_\mathrm{a}} + w_3 \, V \tag{4.13}$$

The convergence of MOO is shown in Fig. 4.13. The design variables are optimized to:

$$[\, l_\mathrm{s} \quad d_\mathrm{r} \quad d_\mathrm{a} \quad l_\mathrm{d} \,]^\mathrm{T} = [\, 6 \quad 25.38 \quad 50 \quad 7 \,]^\mathrm{T} \quad \mathrm{mm} \tag{4.14}$$

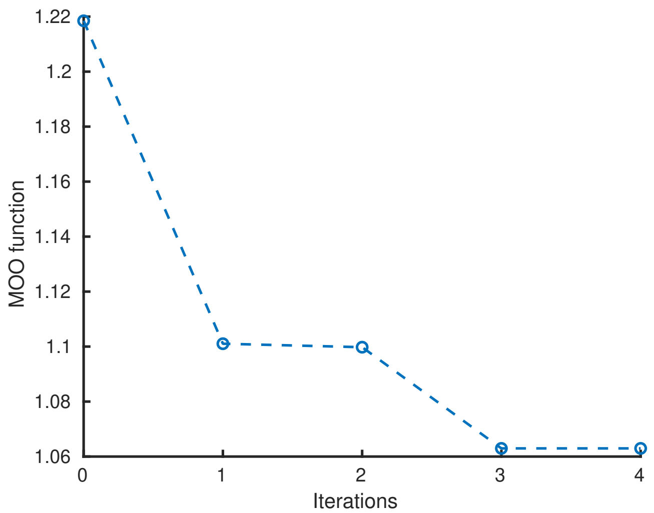

Figure 4.13: MOO function minimization

A surrogate optimization was run for MOO function as well. The results are shown in Fig. 4.14 where the MOO function was minimized to 1.0647 compared to 1.0629 from SQP optimization. The design variables also showed almost the same results.

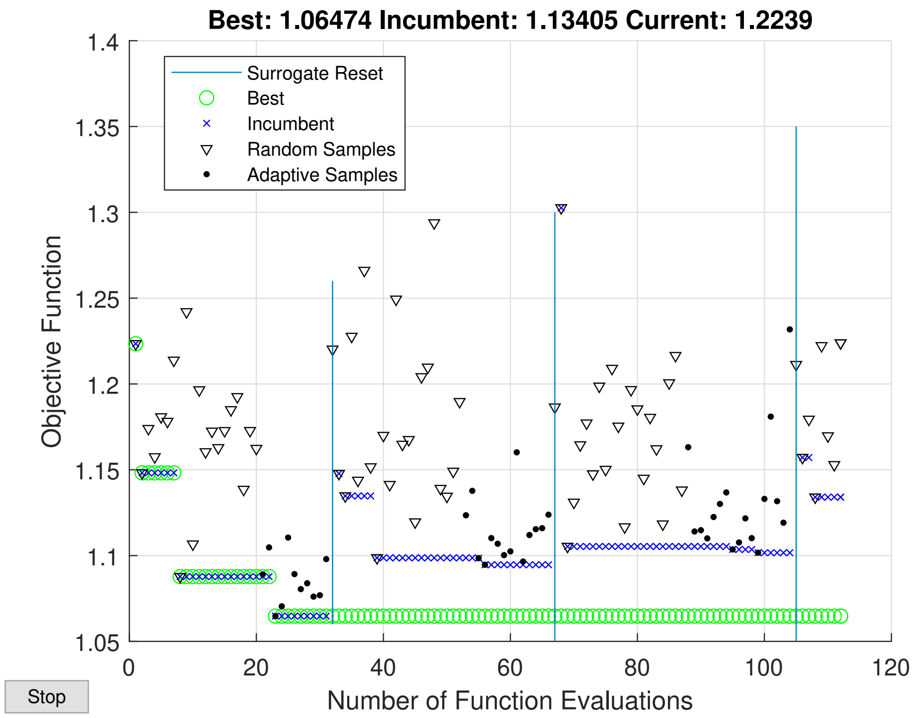

Figure 4.14: MOO function minimization using surrogate optimization

All results of SOO and MOO are summarized in Table 4.3. Based on MOO results, the percent improvements in radial force, axial force, and volume are noted as 11.9, 20.8, and 10.1, respectively.

Table 4.3: Optimization results with weighting coefficients

Parameters	**Radial force f_r**	**Axial force f_a**	**Volume V**
Initial value, f_i	2.1606 N	5.4979 N	1.4x10^{-5} m^3
SOO results, f_i'	2.4946 N	6.6378 N	1.1x10^{-5} m^3
SOO rate, r_i	0.1546	0.2073	0.2157
Normalized rate, $w_{\mathrm{norm},i}$	0.2676	0.3590	0.3734
ND coefficient, $w_{\mathrm{nd},i}$	2.4946	6.6378	92606.5636
Weighting coefficient, w_i	0.6675	2.3828	34582.6271
MOO results	2.417	6.6418	1.24x10^{-5}
Optimization rate (%)	11.86	20.80	10.1

4.6 Summary and Recommendations

This chapter delineated the design and multiobjective performance optimization of the miniaturised combined radial-axial bearing. The micro-milling application requirements define the required rotational speed, machining forces, and the negative stiffness. The component design and material selection are heavily influenced by these requirements. Components including rotor, radial and axial magnetic stators, and conductor coils are initially dimensioned using the 3D FE model developed for this topology.

For the optimization scheme, a gradient-based approach (SQP) is used to first optimize each objective function individually and then a weighted sum multi-objective function is developed and minimized. Next, a surrogate optimization method is used to justify reliance on the results. Based on multiobjective optimization, the objective functions of radial force, axial force, and volume are improved by 11.86, 20.8, and 10.1 percent. A few recommendations about the studies from this chapter are:

- Although surrogate optimization is a global optimization method, a Pareto search is recommended to have more confidence in the results.
- The FE force calculations using COMSOL's built-in function were observed to be nonsmooth. Therefore, another interface of COMSOL, named as *Magnetic Fields (mf)*, was used with quadratic discretization for magnetic scalar and vector potential domains. However, the same nonsmooth behavior of the forces was again noticed. For better convergence with gradient-based optimization methods, it is recommended to opt for a force calculation method which returns smoother variation of forces. The sensitivities using COMSOL's in-built adjoint method and manual perturbation of the dimensions could not be reconciled; a nonsmooth and oscillatory nature of the forces could be the cause.
- The miniaturized design presented in this chapter needs realization in conjunction with a motor installed inside the axial bearing section to prove the practical feasibility of this design.
- Although a safe working current density is selected in this study for a design without forced cooling, a FE-based study of temperature distribution around the permanent magnet positions is recommended to have more confidence that magnets do not experience a temperature above the recommended range.

Considering the future realization of this design, an estimate for temperatures of locally available NdFeB magnets can be found at Manyet, Istanbul [51].

Chapter 5

Slender Rotor Spindle Design

This chapter presents a thorough treatment of the design of the major components needed to realize a slender rotor spindle. The design is accompanied by manufacturing details to be implemented as future work.

5.1 Application Requirements

Similar to the miniaturized combined bearing, the slender rotor spindle is aimed at the application of high-speed micro-milling process. The design of the spindle components follows the application requirements of rotational speed, milling forces, and negative stiffness as already delineated in Section 4.1. Here we only reproduce the relevant details briefly.

- **Rotational speed**: Based on typical micro-milling tool diameter of 200 μm and typical cutting speed of 130 m/min, a theoretical rotational speed of 207,000 rpm (3450 Hz) is required. However, acknowledging that (**1**) the rotational speed limits the rotor diameter due to centrifugal stress; (**2**) enough space on the thrust disc is required to accommodate the axial thrust bearing; a lower rotational speed of 115,000 rpm (1917 Hz) is aimed.
- **Milling forces**: As explained in Section 4.1.2, a vertical slot milling operation with a 200 μm cutting tool, feed rate of 5 μm per tooth, and depth of cut of 5 μm, was considered. The static components of cutting forces were obtained as 0.08 N and 0.05 N along lateral axes. Moreover, a higher static component of 0.5 N acted along the axial axis was found. The dynamic force amplitude stayed around 0.3 N in all directions.
- **Negative stiffness**: Based on the milling forces found above, a controlled

closed-loop bearing stiffness of 1.4×10^5 N/m is aimed to compensate for static cutting forces. As a rule of thumb mentioned by Molenaar [41], a negative bearing stiffness of the same magnitude, or at most one order of magnitude lower, can be selected. Therefore, a negative stiffness in the range 1×10^4 - 1×10^5 N/m is aimed in this study.

5.2 Rotor

The slender rotor for this bearing configuration is designed similarly to the rotor of miniaturized bearing topology in Section 4.3.1. The maximum attainable rotational speed Ω_{max} relates to disc diameter by the relation [44]:

$$\Omega_{\text{max}} = \frac{1}{r}\sqrt{\frac{8\sigma_{\text{o}}}{(\nu+3)\rho}} \tag{5.1}$$

where r is disc radius, σ_{o} is yield strength, ν is the Poisson's ratio, and ρ is the rotor material density. Since ultra-high rotational speeds make the use of electrical steel laminations challenging due to high centrifugal stresses, a solid rotor is used here as done for the rotor of miniaturized bearing topology in Section 4.2. Using ferritic SS of annealed AISI 430F as rotor material with $\sigma_{\text{o}} = 275$ MPa, $\nu = 0.27$, and $\rho = 7750$ kg/m^3, a maximum disc diameter of 48.9 mm is obtained for a rotational speed of 115,000 rpm. However, considering the material inhomogeneities in the rotor material, a factor of safety is applied to select 30 mm as the disc diameter.

Next, the rotor segments facing the radial bearings are dimensioned to have 16 mm of diameter in response to the minimum target diameter of the selected displacement sensors. This diameter can also accommodate typical micro-machining tool shank diameters. The rotor segment for air turbine is kept at 12 mm based on the design of the air turbine. The overall rotor length places the first bending (flexural) mode around 7 times more than the target closed-loop AMB bandwidth of 300 Hz and also out of the operating range as seen in the rotor Campbell diagram drawn in Fig. 5.1. The estimate of bandwidth is taken from Kimman *et al.* [9] and Allaire *et al.* [42]. An in-house and open-source rotordynamic code [39] was used to model the rotor and extract its Campbell diagram. The rotor schematic and CAD model are shown in Fig. 5.2. The relevant parameters of the rotor are listed in Table 5.1.

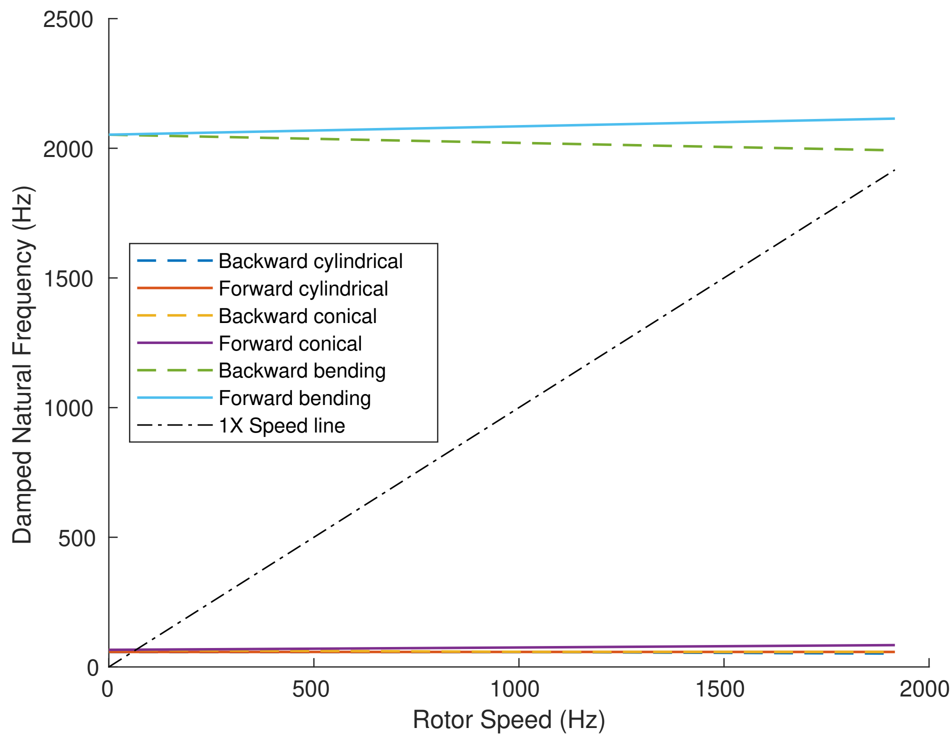

Figure 5.1: Rotor Campbell diagram showing the rigid body and bending modes variation with rotor speed. 1X speed line represents the synchronous excitation line

Table 5.1: Slender rotor parameters

Parameters	**Values**
Total length (mm)	150
Diameter at bearing locations (mm)	16
Diameter (mm)	12
Axial thickness of disc (mm)	3
Diameter of disc (mm)	30
Material	AISI 430F
Weight (N)	2.1

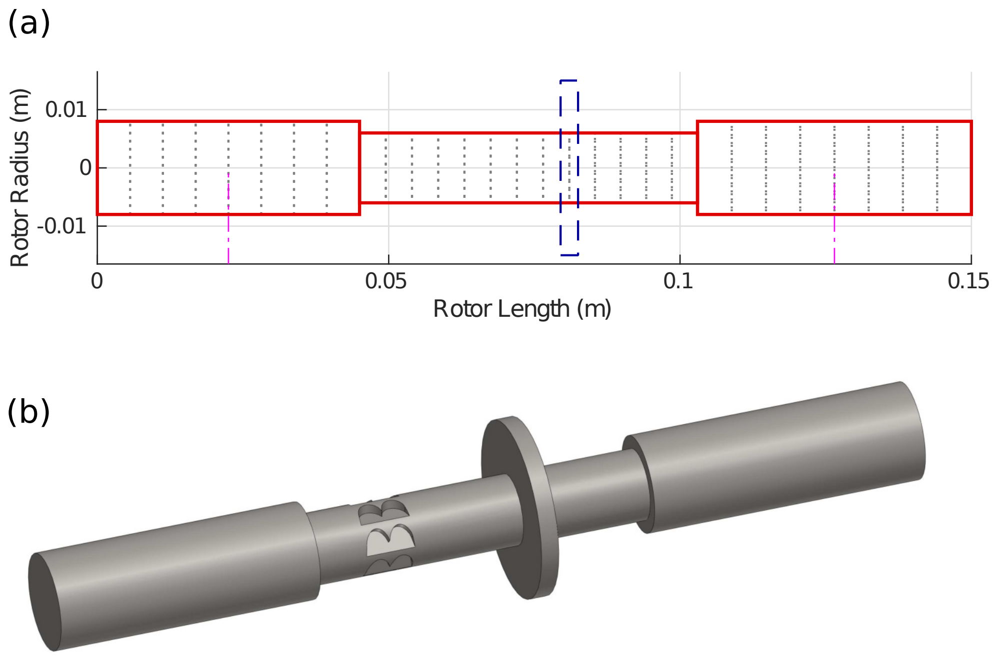

Figure 5.2: Slender rotor geometry: (a) Schematic with dashed blue lines illustrating the thrust disc and vertical dash-dotted lines showing the bearing locations, (b) CAD model

5.3 Air Turbine

In spindles, the most common drive methods for the rotor include electric motors and air turbines. Kimman [52] used a permanent magnet synchronous motor while Park *et al.* [13] utilized an air turbine. For our study, we designed an air turbine to be driven by compressed air. The design method is inspired by work of Li *et al.* [53]. The procedure involves selecting the turbine diameter first while avoiding the super sonic flow. This is followed by torque calculations based on the applied pressure from nozzle connected to the compressor.

Next, the turbine blade profiles on the rotor are drawn by following the procedure given by Solemslie [54]. The turbine blade profiles are shown in Fig. 5.3 and parameters are listed in Table 5.2. The nozzle fixture is shown in Fig. 5.4.

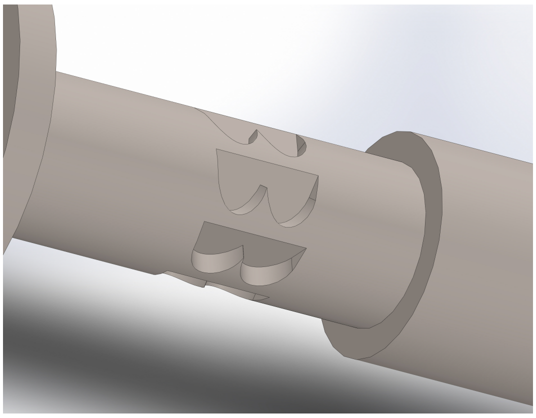

Figure 5.3: Air turbine blades on slender rotor segment

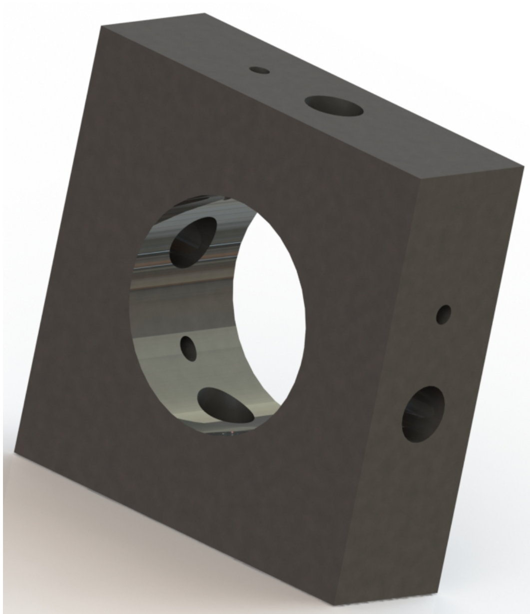

Figure 5.4: Nozzle fixture showing smaller holes as air inlets and larger holes as air outlets

Table 5.2: Air turbine parameters

Parameters	**Values**
Turbine diameter (mm)	12
Pitch diameter (mm)	10
Nozzle diameter (mm)	1.5
Number of nozzles	4
Inlet pressure (MPa)	0.3

5.4 Radial Bearing

The radial bearing for slender rotor configuration is dimensioned in a similar manner to the radial bearing section of the miniaturized topology in Section 4.3.2. Therefore only important details are repeated in this section. The 3D FE model developed in Section 3.2.1.1 is utilised for sizing the bearing and the topology is reproduced here in Fig. 5.5. Operating in the linear range of BH curves of the materials used, *i.e.* up to 1 T, we set bias flux levels at around 0.5 T using the usual rule of thumb [34].

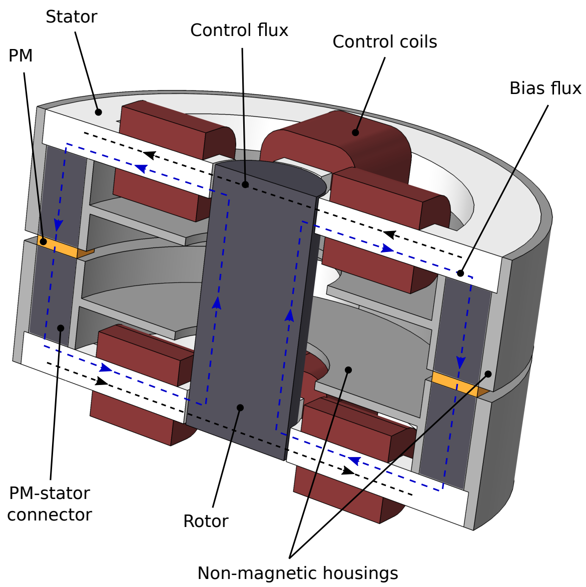

Figure 5.5: Radial bearing half-section view with bias and control flux directions in dashed lines.

Assuming a well-balanced rotor and space for backup bearing, the radial airgap length is kept at 0.3 mm. The NdFeB grade N52 PM blocks, connected to the stator with annealed AISI 430F steel, are used to provide the bias flux. Electrical steel laminations are selected for the stator part. Although the radial machining forces on the tool are limited to a static component of 0.08 N and a dynamic amplitude of almost 0.3 N as discussed in Section 5.1, we generously set the lowest bearing radial load capacity as 14 N accounting for unbalance (considering the rotor weighs 2.1 N) and possible disturbances. Furthermore, radial negative stiffness between 1x10^4 and 1x10^5 Nm^{-1} needs to be ensured.

For these objectives, we manually iterate the stator pole area, coil turns, and applied current. Accordingly, the initial dimensions and key parameters of the radial stator are listed in Table 5.3 and assembly view of the bearing with housings is shown in Fig. 5.6.

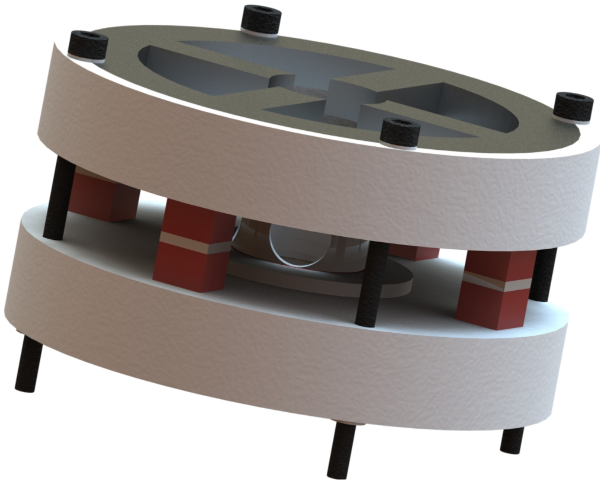

Figure 5.6: Radial bearing assembly with housings and lock nuts

5.4.1 Magnetic flux density norm

To ensure the flux density norm levels do not move towards saturation, we plotted these levels using the FE model for two different sections using the FE model in Figs. 5.7 and 5.8.

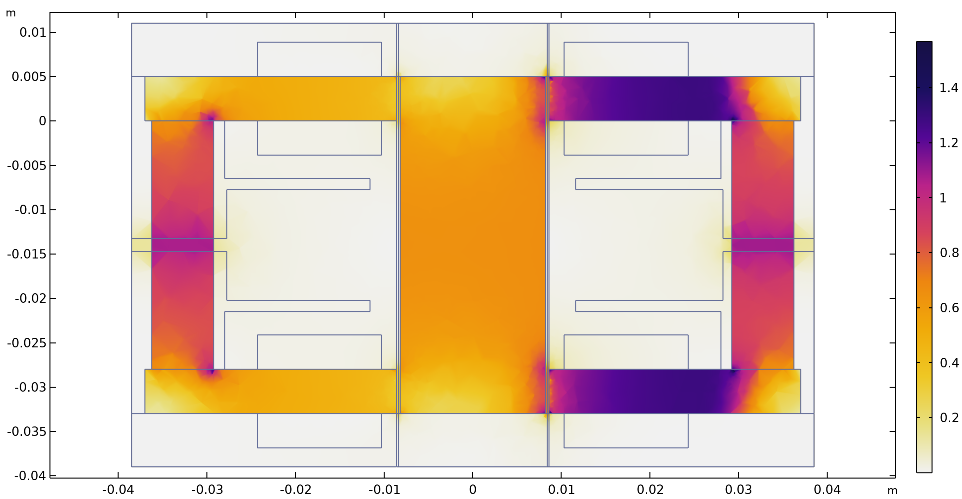

Figure 5.7: Magnetic flux density norm distribution for half section of radial bearing at maximum actuation current.

A few parameters not mentioned in the table are of less significance. For instance, the radial length of poles can be decided based on the space needed by the coils. The

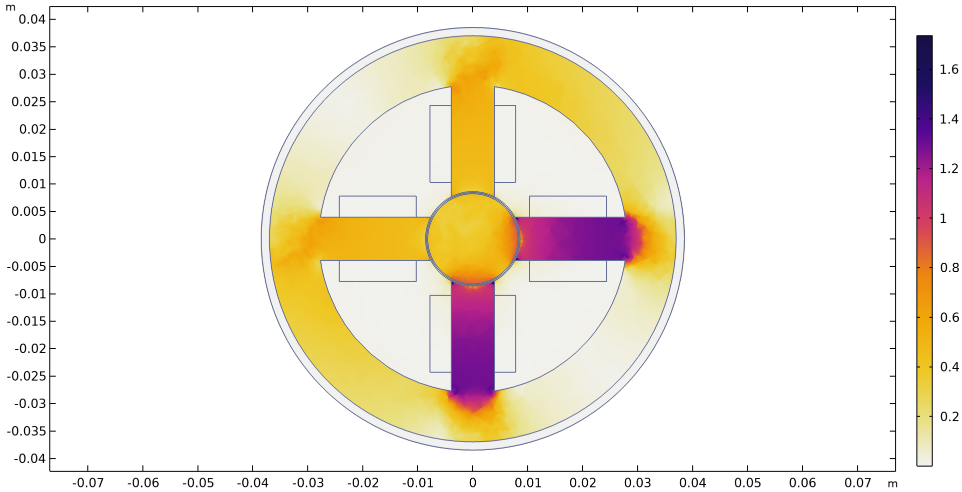

Figure 5.8: Magnetic flux density norm distribution for radial stator at maximum actuation current.

Table 5.3: Radial bearing parameters

Parameters	**Values**
Pole shoe surface area (mm^2)	40.788
Airgap length (mm)	0.3
PM cross-sectional area (mm^2)	96.788
Coil wire size	AWG 16 (1.291 mm diameter)
Number of coil turns per pole	30
Maximum coil current (A)	3
PM remanent flux density (T)	1.44

radial thickness of radial stator can be selected in a way so that magnetic saturation does not occur when maximum current is applied.

5.5 Axial Thrust Bearing

Based on the linearized force derived for double-sided reluctance actuators in differential driving mode in Section 3.2.2, the axial thrust bearing is dimensioned in this section. This bearing consists of two u-shaped reluctance actuators with coils wound tangentially. The linearized force acting on the thrust disc is given by:

$$F_{\rm a} = K_{\rm i} i_{\rm p} + K_{\rm z} z \tag{5.2}$$

where $K_{\rm i}$ and $K_{\rm z}$ are open-loop current gain (force-current dependency) and negative stiffness (force-displacement dependency or open-loop stiffness), respectively, and are given by (refer to Section 3.2.2 for notations):

$$K_{\rm i} = \frac{\mu_{\rm o} n^2 A_{\rm p} i_{\rm b}}{l_{\rm o}^2} \tag{5.3}$$

$$K_{\rm z} = \frac{\mu_{\rm o} n^2 A_{\rm p} i_{\rm b}^2}{l_{\rm o}^3} \tag{5.4}$$

The relevant application requirements from Section 5.1 include: (**1**) static component of milling force at 0.5 N, dynamic force amplitude of 0.3 N, and weight of the rotor at 2.1 N, (**2**) negative stiffness in the range 1×10^4 - 1×10^5 N/m. The bearing is dimensioned iteratively to meet these requirements. The airgap length is kept the same as that for radial bearing, *i.e.* 0.3 mm. The CAD model of one axial actuator is shown in Fig. 5.9. The final bearing parameters are listed in Table 5.4.

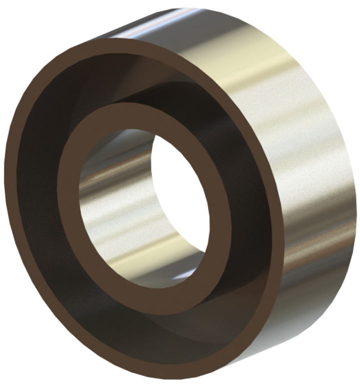

Figure 5.9: Rendered CAD image of axial thrust actuator

Table 5.4: Axial thrust bearing parameters

Parameters	**Symbols**	**Values**
Pole shoe surface area (mm^2)	A_p	70
Airgap length (mm)	l_a	0.3
Coil turns (per actuator)	n	35
Bias current (A)	i_b	2
Open loop current gain (N/A)	K_i	9.57
Negative stiffness (N/m)	K_z	6.38x10^4

5.6 Assembly

All major components designed in this chapter are assembled in Fig. 5.10. Two radial bearings control the rotor in the radial direction. Beneath the top radial bearing, the nozzles are present for compressor connection. Two axial bearing actuators are placed near the rotor thrust disc. Vibration resistant locknuts with wedge-locking washers are used to hold the components together. The material for the side plates is aluminum for strength and low weight. The recommendations for manufacturing processes are given in the recommendations section of this chapter.

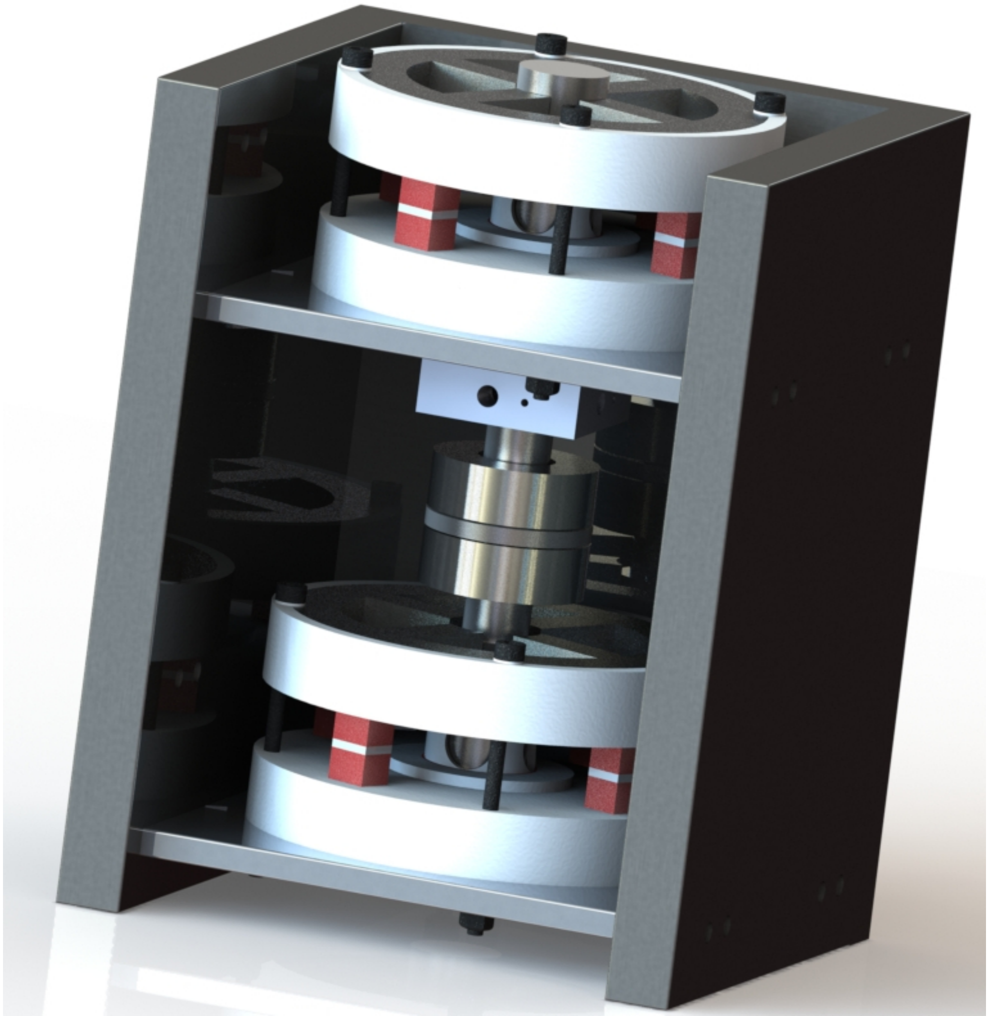

Figure 5.10: Rendered CAD assembly of slender rotor spindle

5.7 Summary and Recommendations

The detailed design of the slender rotor spindle is discussed in this chapter. Micro-milling application requirements of rotational speed, milling forces, and negative stiffness derive the components design process with the aid of analytical and FE models. The component design for rotor, air turbine, radial bearing, and axial bearing were described. The selection of materials was justified based on magnetic properties and strength. For manufacturing the spindle, a few recommendations can be noted:

- Round bar material for the rotor needs to be acquired in annealed condition for better magnetic performance. After general machining, a grinding process is required to give better tolerance and surface for displacement sensor target.

- The laminated electrical steel for the radial bearing stator needs to be cut with electrical discharge machining (EDM) to give the best performance during bearing operation.
- Fiber lock nuts resist loosening due to vibration and torque. Additionally wedge-locking washers are recommended.

Chapter 6

Conclusion and Recommendations

The studies presented in this thesis are concluded here along with the recommendations for future work.

6.1 Concluding Remarks

This thesis focuses primarily on four areas: (**1**) development of spectral element method algorithm, (**2**) the modelling methods for rotors and active magnetic bearings, (**3**) design of spindle components based on application requirements, (**4**) the multiobjective performance optimization of magnetic bearings.

To study the speed dependent dynamic behavior of high-speed rotors, a spectral element method is explained with the background theory of Timoshenko beam and Chebyshev polynomials. The algorithm of the developed code explains the primary steps from user input to the final evaluation of eigenvalue problem. The approach divides the rotor/beam into segments based on change in diameter. Afterwards, a segment-by-segment assembly is initiated to complete the global mass, stiffness, and coriolis matrices.

Once the rotordynamic model is built, the models for active magnetic bearings are developed to dimension and optimize the bearings. Two different spindle configurations were studied, a miniaturised combined radial-axial bearing and conventional topologies of separate radial and axial bearings. Acknowledging the accuracy of finite element (FE) models over that of analytical ones, both topologies are modelled with FE approach. However, considering the simple geometry of axial bearing in conventional bearing topologies, an analytical model based on reluctance force is developed.

With all the models developed, the application requirements of the micromilling process, namely rotational speeds, milling forces, and negative stiffness, are imposed on the design and material selection for the spindle components of both bearing topologies.

For the optimization scheme, a gradient-based approach (SQP) is used to first optimize each objective function individually and then a weighted sum multi-objective function is developed and minimized. As a result of multi-objective optimization, the objective functions of radial force, axial force, and volume are improved by 11.86, 20.80, and 10.1 percent in the miniaturised combined radial-axial bearing. A surrogate optimization (nongradient global optimization method) is also performed to increase confidence in the results.

For one of the spindle topologies, the design of the drive method of air turbine is also conducted to meet the rotational speed and torque requirements of the machining process. Finally, as assembled design is presented with recommendations on the next steps of realization of the spindle setup.

6.2 Recommendations for Future Work

For the next steps including the realization of the spindle system, a few recommendations are listed below.

- The force dependence on dimensional parameters was found to be very non-smooth in the finite element model. In such a case, opting for non-gradient based optimization methods may be a better approach.
- A global optimization approach is preferred to verify the results from the local optimization methods. A multiobjective Pareto search is recommended.
- For manufacturing, a round bar for the rotor needs to be acquired in annealed condition for a better magnetic performance. After initial machining, a grinding process is required to give better tolerance and surface conditions, especially at the rotor segments inside the radial bearing sections. A smooth ground surface is specifically needed for displacement sensors to output high-quality rotor position signals without reduced levels of noise.
- The laminated electrical steel for the radial bearing stator needs to be cut with electrical discharge machining (EDM) to give the best performance during

bearing operation.

- Vibration resistant lock nuts should be used to prevent the loosening of the components.
- In most cases, the axial bearings are biased by coil current. However, recent literature shows promise of using permanent magnets to provide bias flux. Such an arrangement has resulted in significant improvements in the actuator bandwidth [42].
- The miniaturized design presented in this chapter needs realization in conjunction with a motor installed inside the axial bearings to prove the feasibility of this design practically.

Bibliography

[1] K. Ehmann, D. Bourell, M. Culpepper, and T. Hodgson, "International assessment of research and development in micromanufacturing," tech. rep., 2005.

[2] M. A. Câmara, J. C. Rubio, A. M. Abrão, and J. P. Davim, "State of the Art on Micromilling of Materials, a Review," *Journal of Materials Science and Technology*, vol. 28, pp. 673–685, 8 2012.

[3] B. Z. Balázs, N. Geier, M. Takács, and J. P. Davim, "A review on micro-milling: recent advances and future trends," 1 2021.

[4] European-Commission, "Horizon Europe - Work Programme 2021-2022: Digital, Industry and Space," tech. rep., 2021.

[5] S. P. L. Kumar, J. Jerald, S. Kumanan, and R. Prabakaran, "A Review on Current Research Aspects in Tool-Based Micromachining Processes," *http://dx.doi.org/10.1080/10426914.2014.952037*, vol. 29, pp. 1291–1337, 12 2014.

[6] X. Liu, R. E. DeVor, S. G. Kapoor, and K. F. Ehmann, "The mechanics of machining at the microscale: Assessment of the current state of the science," *Journal of Manufacturing Science and Engineering, Transactions of the ASME*, vol. 126, pp. 666–678, 11 2004.

[7] S. Filiz, C. M. Conley, M. B. Wasserman, and O. B. Ozdoganlar, "An experimental investigation of micro-machinability of copper 101 using tungsten carbide micro-endmills," *International Journal of Machine Tools and Manufacture*, vol. 47, pp. 1088–1100, 6 2007.

[8] L. Xie, S. D. Brownridge, O. B. Ozdoganlar, and L. E. Weiss, "The viability of micromilling for manufacturing mechanical attachment components for medical applications," *Transactions of the North American Manufacturing Research Institute of SME*, vol. 34, pp. 445–452, 2006.

[9] M. H. Kimman, H. H. Langen, and R. H. Munnig Schmidt, "A miniature milling spindle with Active Magnetic Bearings," *Mechatronics*, vol. 20, no. 2, pp. 224–235, 2010.

[10] B. Bediz, B. Arda Gozen, E. Korkmaz, and O. Burak Ozdoganlar, "Dynamics of ultra-high-speed (UHS) spindles used for micromachining," *International Journal of Machine Tools and Manufacture*, vol. 87, pp. 27–38, 2014.

[11] J. Chae, S. S. Park, and T. Freiheit, "Investigation of micro-cutting operations," *International Journal of Machine Tools and Manufacture*, vol. 46, pp. 313–332, 3 2006.

[12] R.-M. Lee and T.-C. Chen, "Adaptive Control of Active Magnetic Bearing against Milling Dynamics," *Applied Sciences*, vol. 6, p. 52, 2 2016.

[13] J. K. Park, J. H. Kyung, W. C. Shin, and S. K. Ro, “A magnetically suspended miniature spindle and its application for tool orbit control,” *International Journal of Precision Engineering and Manufacturing*, vol. 13, no. 9, pp. 1601–1607, 2012.

[14] C. R. Knospe, “Active magnetic bearings for machining applications,” *Control Engineering Practice*, vol. 15, pp. 307–313, 3 2007.

[15] M. H. Kimman, *Design of a Micro Milling Setup with an Active Magnetic Bearing Spindle.* PhD thesis, TU Delft, 2010.

[16] W.-L. Lee, *Aufbau und Regelung homopolarer Magnetlagersysteme.* PhD thesis, Institut für Regelungstechnik, TU-Braunschweig, 2002.

[17] B. Bediz and O. B. Ozdoganlar, “Rotational dynamics of micro-scale cutting tools,” *Precision Engineering*, vol. 60, pp. 1–11, 11 2019.

[18] H. D. Nelson and J. M. McVaugh, “The Dynamics of Rotor-Bearing Systems Using Finite Elements,” *Journal of Engineering for Industry*, vol. 98, pp. 593–600, 5 1976.

[19] H. D. Nelson, “A Finite Rotating Shaft Element Using Timoshenko Beam Theory,” *Journal of Mechanical Design*, vol. 102, pp. 793–803, 10 1980.

[20] Y. Cao and Y. Altintas, “A General Method for the Modeling of Spindle-Bearing Systems,” *Journal of Mechanical Design*, vol. 126, pp. 1089–1104, 11 2004.

[21] G. Bramerdorfer, A. C. Zavoianu, S. Silber, E. Lughofer, and W. Amrhein, “Possibilities for Speeding Up the FE-Based Optimization of Electrical Machines-A Case Study,” *IEEE Transactions on Industry Applications*, vol. 52, no. 6, pp. 4668–4677, 2016.

[22] A. Ertürk, H. N. Özgüven, and E. Budak, “Analytical modeling of spindle–tool dynamics on machine tools using Timoshenko beam model and receptance coupling for the prediction of tool point FRF,” *International Journal of Machine Tools and Manufacture*, vol. 46, pp. 1901–1912, 12 2006.

[23] A. Ertürk, H. N. Özgüven, and E. Budak, “Effect analysis of bearing and interface dynamics on tool point FRF for chatter stability in machine tools by using a new analytical model for spindle–tool assemblies,” *International Journal of Machine Tools and Manufacture*, vol. 47, pp. 23–32, 1 2007.

[24] H. Arvin, Y. Q. Tang, and A. Ahmadi Nadooshan, “Dynamic stability in principal parametric resonance of rotating beams: Method of multiple scales versus differential quadrature method,” *International Journal of Non-Linear Mechanics*, vol. 85, pp. 118–125, 10 2016.

[25] E. Cigeroglu and H. Samandari, “Nonlinear free vibrations of curved double walled carbon nanotubes using differential quadrature method,” *Physica E: Low-dimensional Systems and Nanostructures*, vol. 64, pp. 95–105, 11 2014.

[26] B. Bediz, L. A. Romero, and O. Burak Ozdoganlar, "Three dimensional dynamics of rotating structures under mixed boundary conditions," *Journal of Sound and Vibration*, vol. 358, pp. 176–191, 2015.

[27] B. Yagci, S. Filiz, L. L. Romero, and O. B. Ozdoganlar, "A spectral-Tchebychev technique for solving linear and nonlinear beam equations," *Journal of Sound and Vibration*, vol. 321, no. 1-2, pp. 375–404, 2009.

[28] J. Boyd, *Chebyshev and Fourier spectral methods.* 2001.

[29] F. Betschon, *Design Principles of Integrated Magnetic Bearings.* PhD thesis, ETH Zurich, 2000.

[30] B. Han, Q. Xu, and Q. Yuan, "Multiobjective Optimization of a Combined Radial-Axial Magnetic Bearing for Magnetically Suspended Compressor," *IEEE Transactions on Industrial Electronics*, vol. 63, no. 4, pp. 2284–2293, 2016.

[31] Y. Le and K. Wang, "Design and Optimization Method of Magnetic Bearing for High-Speed Motor Considering Eddy Current Effects," *IEEE/ASME Transactions on Mechatronics*, vol. 21, no. 4, pp. 2061–2072, 2016.

[32] G. Ding, Z. Zhou, Y. Hu, and D. He, "FEA-based optimal design of the radial magnetic bearings in magnetic suspended hard disk drive," *Proceedings of the 2nd IEEE/ASME International Conference on Mechatronic and Embedded Systems and Applications, MESA 2006*, 2006.

[33] S. Cheng, M. W. Olles, A. F. Burger, and S. W. Day, "Optimization of a hybrid magnetic bearing for a magnetically levitated blood pump via 3-D FEA," *Mechatronics*, vol. 21, no. 7, pp. 1163–1169, 2011.

[34] S. Y. Yoon, Z. Lin, and P. E. Allaire, *Control of Surge in Centrifugal Compressors by Active Magnetic Bearings.* Springer, 2013.

[35] X. Zhang, D. Thompson, and X. Sheng, "Differences between Euler-Bernoulli and Timoshenko beam formulations for calculating the effects of moving loads on a periodically supported beam," *Journal of Sound and Vibration*, vol. 481, p. 115432, 9 2020.

[36] L. Meirovitch, *Fundamentals of Vibrations.* Waveland Press, 2010.

[37] S. Filiz, O. B. Ozdoganlar, and L. A. Romero, "An analytical model for micro-endmill dynamics," *Journal of Vibration and Control*, vol. 14, no. 8, pp. 1125–1150, 2008.

[38] D. Gottlieb and S. Orszag, *Numerical Analysis of Spectral Methods: Theory and Applications.* SIAM, 1977.

[39] K. S. Ahmed and S. Mushtaq Ahmad, "VibronRotor, an opensource rotordynamic code: Development and benchmarking," *Measurement*, 2019.

[40] COMSOL, "The AC/DC Module User's Guide," tech. rep., 2020.

[41] L. Molenaar, *A novel planar magnetic bearing and motor configuration applied in a positioning stage.* PhD thesis, TU Delft, 2000.

[42] P. Allaire, B. Nichols, T. Dimond, J. Cao, and S. Mushi, "Low Cost Active Magnetic Bearings-Concepts and Examples," in *ISMB15*, 2017.

[43] T. A. Dow, E. L. Miller, and K. Garrard, "Tool force and deflection compensation for small milling tools," *Precision Engineering*, vol. 28, pp. 31–45, 1 2004.

[44] R. Larsonneur, *Design and control of active magnetic bearing systems for high speed rotation.* PhD thesis, ETH Zurich, 1990.

[45] A. Filatov, L. Hawkins, and P. McMullen, "Homopolar permanent-magnet-biased actuators and their application in rotational Active Magnetic Bearing systems," *Actuators*, vol. 5, no. 4, 2016.

[46] D. R. Gauder, M. H. Froning, R. J. White, and A. E. Ray, "Elevated temperature study of Nd-Fe-B–based magnets with cobalt and dysprosium additions," *Journal of Applied Physics*, vol. 63, p. 3522, 6 1998.

[47] M. Sagawa, K. Hiraga, H. Yamamoto, and Y. Matsuura, "Permanent magnet materials based on the rare earth-iron-boron tetragonal compounds (invited)," *IEEE Transactions on Magnetics*, vol. 20, no. 5, pp. 1584–1589, 1984.

[48] W. K. Khoo, S. D. Garvey, and K. Kalita, "The specific load capacity of radial-flux radial magnetic bearings," *IEEE Transactions on Magnetics*, vol. 43, pp. 3293–3300, 7 2007.

[49] A. Borisavljevic, M. H. Kimman, P. Tsigkourakos, H. Polinder, H. H. Langen, R. Munnig Schmidt, and J. A. Ferreira, "Motor drive for a novel high-speed micro-milling spindle," *IEEE/ASME International Conference on Advanced Intelligent Mechatronics, AIM*, pp. 1492–1497, 2009.

[50] A. Borisavljević, *Limits, Modeling and Design of High-Speed Permanent Magnet Machines.* PhD thesis, TU Delft, 2011.

[51] Manyet, "NEODYUM MIKNATIS," tech. rep., Istanbul.

[52] M. H. Kimman, H. H. Langen, J. Van Eijk, and R. Munnig Schmidt, "Design and realization of a miniature spindle test setup with active magnetic bearings," in *IEEE/ASME International Conference on Advanced Intelligent Mechatronics, AIM*, pp. 1–6, 2007.

[53] W. Li, M. Liu, Y. H. Ren, and Q. Chen, "A high-speed precision micro-spindle use for mechanical micro-machining," *International Journal of Advanced Manufacturing Technology*, vol. 102, no. 9-12, pp. 3197–3211, 2019.

[54] B. W. Solemslie, *Dissertation: Experimental methods and design of a Pelton bucket.* PhD thesis, 2016.

Appendix A

MATLAB code listings

```
% Main optimization script

clear all; clc;
format long;
tic                       % Timer starts

% Design variables with initial values [m]
    s_t    = 0.0045;      % radial stator length
    disc_d = 0.024;       % Rotor disc diameter
    ax_dia = 0.058;       % Axial stator diameter
    disc_l = 0.008;       % Rotor disc length
    xo = [ s_t disc_d ax_dia disc_l  ];     % Design vector

% Linear constraints
% [Left empty: No such constraints used in study]
    A   = [];             % Inequality linear constraint
    B   = [];
    Aeq = [];             % Equality linear constraint
    Beq = [];

% Bounds considering physical limitations of spindle test-rig
    lb = [ 0.003  0.0236  0.050  0.007 ];   % Lower bounds [m]
    ub = [ 0.005  0.0272  0.058  0.010 ];   % Upper bounds [m]

% Model loading
    model = mphload ('COMSOL model filename.mph');

% Objective function and constraint definition
    obj_func = @(x) comsol_obj_MOO(x,model);
    nonlcon  = @(x) comsol_cons(x);

% Optimizer setup and call [example settings]
    opts = optimoptions('fmincon','Algorithm','sqp'...
    ,'StepTolerance',1e-4,'FunctionTolerance',1e-3...
    ,'OptimalityTolerance',1e-3,'DiffMinChange',0.4e-3...
    ,'DiffMaxChange',1,'ConstraintTolerance',1e-4...
    ,'PlotFcn','optimplotfval');

    opts.Display = 'iter';     % Print the iteration details

```

```
    [xopt,fval,exitflag,output,lambda,grad,hessian] =...
    fmincon( obj_func ,xo,A,B,Aeq,Beq,lb,ub,nonlcon,opts );

toc                              % Timer stops
```

```
% Function file to feed updated design variables to COMSOL

% Function definition
    function [MOO_obj] = comsol_obj_MOO(x,model)

% Assign the updated design variables
    s_t    = x(1);
    disc_d = x(2);
    ax_dia = x(3);
    disc_l = x(4);

% Write the design variables to COMSOL model file
    model.param.set('s_t', s_t);
    model.param.set('disc_d', disc_d);
    model.param.set('ax_dia', ax_dia);
    model.param.set('disc_l', disc_l);

% Run the study in COMSOL model file
    model.study('std1').run;

% Read the objective function values from COMSOL model file.
% Relevant dataset can be found using COMSOL Model Navigator
% in MATLAB applications
    forcex = -mphglobal(model,'rmm2.Forcex_0'...
    ,'dataset','dset101')

    forcez = mphglobal(model,'rmm2.Forcez_0'...
    ,'dataset','dset101')

    Vol = mphglobal(model,'intop1_PM(1)+intop2_rotor(1)...
    +intop3_rs(1)+intop4_as(1)','dataset','dset101')

    MOO_obj = 0.355247*(1/forcex) + 2.520790*(1/forcez)...
    +  43295.312256*Vol
```

Finally, a similar function file can be written for constraints.